FEMTOSECOND PULSE LASER MODIFICATION AND TERAHERTZ TIME DOMAIN SPECTROSCOPY OF YTTRIUM ALUMINUM GARNET TRANSPARENT CERAMICS

Daniel Steere

A THESIS
SUBMITTED TO THE FACULTY OF

ALFRED UNIVERSITY

IN PARTIAL FULFILLMENT OF THE REQUIREMENTS
FOR THE DEGREE OF

MASTER OF SCIENCE

IN

MATERIALS SCIENCE AND ENGINEERING

ALFRED, NEW YORK

February 2016

FEMTOSECOND PULSE LASER MODIFICATION AND TERAHERTZ TIME DOMAIN SPECTROSCOPY OF YTTRIUM ALUMINUM GARNET TRANSPARENT CERAMICS

BY

DANIEL STEERE

B.S. ALFRED UNIVERSITY 2011

SIGNATURE OF AUTHOR_____

APPROVED BY _____

DR. S.K. SUNDARAM, ADVISOR

_____

DR. WILLIAM CARLSON, ADVISORY COMMITTEE

_____

DR. YIQUAN WU, ADVISORY COMMITTEE

_____

CHAIR, ORAL THESIS DEFENSE

ACCEPTED BY _____

DOREEN D. EDWARDS, DEAN
KAZUO INAMORI SCHOOL OF ENGINEERING

ACKNOWLEDGMENTS

I owe much to many people for their support, encouragement, and contributions. There was not a single aspect of this work that could have been done without help at some point along the way. Various members of the Alfred University staff were extremely helpful, especially Dave Green who machined many custom parts for me, Katie Decker who helped with all the administrative aspects, Beverly Crowell who always found the books and articles I needed, and many others. I'm thankful to Alfred University for providing the opportunity to work as a GA to fund my tuition, and to Dr. Carlson for allowing me to be the GA for his MATLAB class, which was a lot of fun. Dimitri Papoutzis was instrumental in achieving proper operation of the femtosecond pulse laser, and was a great teacher of both theoretical and practical knowledge about continuous wave and mode-locked lasing. Priyatham Tumorogoti was always there to help run laser experiments, GIXRD, and troubleshoot problems when things didn't go as expected. Phil Taday and Satya Ganti were both extremely helpful with the Terahertz Spectroscopy system. I'd like to thank all of my lab mates, Ruhil Dongol, Priyatham Tumorogoti, Braeden Clark, Kameron Chambliss, and Diksha Kini. Thanks to Braeden Clark for making beautiful YAG crystal structure diagrams. Gerry Wynick took care of all the SEM work, and offered a lot of good advice both about experiments and life in general. I am thankful for the opportunity to work with George Keith and Gary Del Regno during my time as an undergrad and for all the guidance they have given me over the years.

I would like to thank Dr. Sundaram for providing me with the opportunity to work with such interesting and challenging technology, and to diversify my knowledge of both ceramics, and optical physics. I thank God for creating the fundamental framework for such interesting phenomena that are well outside the range of my understanding. Finally I would like to thank my parents, Tom and Susan Steere, for supporting me throughout all of my endeavors, especially in education.

TABLE OF CONTENTS

Page

LIST OF TABLES

Page

LIST OF FIGURES

Page

ABSTRACT

A femtosecond pulse laser was used to investigate the effects of ultra-short pulses of broadband infrared radiation on single crystals and polycrystalline ceramics of yttrium aluminum garnet (YAG), both pure and doped with neodymium. Transparent YAG responded by generating colored light in the visible spectrum, while opaque ceramics exhibited localized densification and ablation. In addition to the physical modification of the microstructure, the femtosecond pulse laser was used to preferentially segregate yttrium atoms within the optical interaction volume of the YAG material. This demonstrates that fs-pulse lasers can be used to preferentially modify the microstructural and chemical properties of dense ceramic materials.

Terahertz time-domain spectroscopy (THz-TDS) was also employed to characterize the dielectric properties of YAG compositions synthesized with precisely controlled and varying stoichiometric atomic ratios. A correlation between the x-ray diffraction (XRD) and THz-TDS data indicated that chemical variation in the YAG solid solution had an effect on the dielectric properties; in yttrium rich compositions, phases of $YAlO_3$ formed while compositions rich in aluminum, phases of Al_2O_3 formed. The precipitation of these phases rendered the material inhomogeneous resulting in a significant change in the optical and dielectric properties due to the composite nature of the material.

YAG ceramics were synthesized with a range of bulk densities, grain sizes, and pore volumes to investigate the effect of microstructure on the THz properties. Bulk density was the dominant factor, exhibiting a linear relationship between density absorption coefficient, real dielectric constant, and refractive index. THz-TDS measurements were also performed at a range of temperatures between 293K and 493K which showed that above 350K there is linear relationship between THz absorption and temperature.

I. INTRODUCTION

Yttrium Aluminum Garnet (YAG) is a well-known and desirable laser gain material due to its stability, low-thermal expansion, hardness, optical isotropy and transparency, low-acoustic loss, high threshold for optical damage, and ability to be doped with rare earth elements[1,2]. YAG has a complex cubic crystal structure, challenging interpretation of its optical behavior in certain parts of the electromagnetic spectrum, e.g., terahertz (THz) frequencies. Figure 1 shows the crystal structure of YAG. It contains three different oxygen polyhedral. Y^{3+} ions occupy the dodecahedral sites with Al^{3+} ions occupying the octahedral and tetrahedral sites in a ratio of 2:3. This arrangement is due to the difference in the ionic radii between O^{2-} (1.4 Å), Y^{3+} (1.281 Å) and Al^{3+} (0.51 Å). Trivalent rare earth ions can replace Y^{3+} ions to a small degree due to the similarity in ionic radii. Nd^{3+} (ionic radius 1.323 Å) is the most frequently used dopant for laser gain applications.[3]

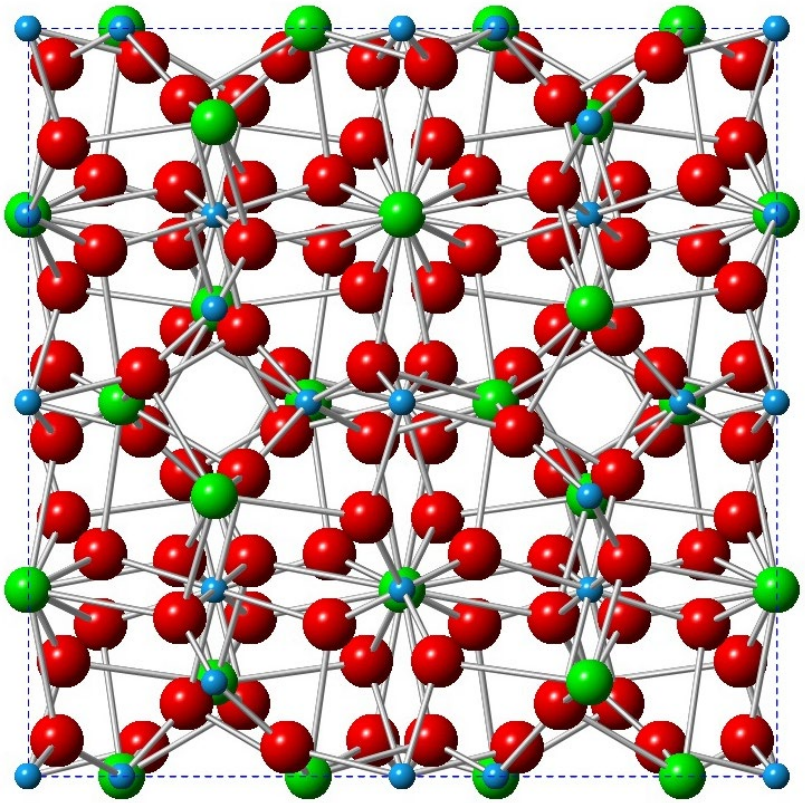

A.

Figure 1. Crystal structure of YAG viewed along the [001] direction. Yttrium is represented by green balls, aluminum by blue, and oxygen by red.

Neodymium (Nd)-doped YAG is the most commonly used YAG material for lasing applications due to its high efficiency and the relative ease of incorporating neodymium atoms into the YAG lattice compared to doping with other rare earth elemenst.[4-7] Nd-doped YAG single crystals fabricated by the Czochralski method are widely used as a solid-state laser gain material but are very difficult to dope homogeneously with neodymium to concentrations above 1% because of the high effective segregation coefficient of elemental neodymium.[8] Nd:YAG crystals fluoresce most strongly between 1.05 μm and 1.08 μm, with the strongest Nd^{3+} emission occurring at 1.0633 μm. At dopant concentrations up to 3 atomic percent Nd, the fluorescence decay time is around 200 μsec, while above 6 atomic % the fluorescence lifetime decreases dramatically, perhaps due to Nd-Nd interactions.

Nd-doped YAG transparent ceramics have garnered interest because of their potential advantages over traditionally grown Nd:YAG single crystals. These advantages

include lower manufacturing cost, higher dopant concentrations without degradation of the optical quality, and the possibility of direct composite fabrication.[9] Scattering caused by pores, grain boundaries, and defects is one of the most important issues involved in using transparent ceramics for optical applications, so a great deal of research has been done to improve the optical properties through better control of the microstructure.[10] Vacuum reaction sintering, high pressure sintering,[11] Sol-gel processing,[12] and spark plasma sintering[13-15] have been investigated as ways to produce transparent ceramic Nd:YAG that is free of defects and secondary phases.

Bulk optical damage thresholds have been measured for doped and undoped YAG ceramics and single crystals using nanosecond pulse lasers with varying pulse durations. At pulse durations of 4 nanosecond (ns) emitting at 1064 nm, damage threshold values of 100±10 J/cm^2 are reported for undoped ceramic and single crystal, while for 0.7% Nd-doped ceramic and single crystal the damage threshold reported is 110±10 J/cm^2.[16]

Multiple-pulse damage thresholds by 8 ns pulses of 1064 nm light have been reported for ceramic YAG doped with 0 to 8% Nd. For dopant levels of 4% and less the reported damage threshold is 50 GW/cm^2 (400 J/cm^2). At 8% dopant concentration, the transparency decreases, resulting in a damage threshold a factor of five lower.[17] Using 9.9 ns, 1064 nm pulses, Do and Smith[29] have shown that the breakdown thresholds are deterministic (consistent under equal conditions) rather than statistical (dependent upon probability) with multiple-pulse thresholds between 1.1 and 2.2 kJ/cm^2. The authors have found a cumulative damage effect leading to a reduced damage threshold for multiple pulses and different dopants result in substantial variation in damage thresholds. For Nd-doped YAG ceramics, 1100 J/cm^2 is the lowest multiple-pulse damage threshold value.

Femtosecond (fs) pulse lasers have several major advantages for micromachining compared to lasers operating with longer pulse durations. Short pulse lasers have been used for color center formation in glass,[18] creation of ablation patterns on semiconductors,[19-21] ablation and fragmentation to synthesize nanoparticles,[22] ablation and white light super-continuum generation in transparent materials,[23-26] and ablation in ceramics.[27,28] They are especially suited for the fabrication of photonic devices in transparent bulk materials that do not absorb linearly at fs laser wavelengths. Three advantages of fs pulse lasers in micromachining transparent materials:[29]

1) Damage is localized in the focal volume of the laser beam due to the non-linear nature of the absorption. This restriction of damage allows micromachining in three dimensions, by adjusting the position of the target area relative to the focal volume of the laser beam.
2) The nonlinear absorption process is independent of the material, allowing different materials to be machined while combined into multilayered architectures.
3) Interconnects can be fabricated separately making an 'optical motherboard.'

THz time-domain spectroscopy (THz-TDS) is a spectroscopic technique utilizing long wavelength (millimeter) radiation to measure the bulk dielectric properties of materials in the frequency range of approximately 300 - 3000 GHz. To the best of our knowledge, no extensive THz data on YAG crystal or ceramics is reported in the literature.

This thesis will focus on the fabrication, fs laser modification, and novel characterization of doped and un-doped yttrium aluminum garnet (YAG) ceramics and single crystals (YAG). A fs pulse laser is used to perform surface modification, and THz-TDS and other well-established techniques have been used to characterize these materials. The goal is to test two hypotheses: i) focused fs pulse laser radiation will be sufficiently powerful to ablate or otherwise modify transparent or opaque YAG materials and ii) chemistry and other physical properties of YAG ceramics will have an effect on the dielectric properties in the THz frequency regime.

II. BACKGROUND

A. FEMTOSECOND PULSE LASER

I. Laser Introduction

The term "laser" originated as an acronym for *Light Amplification by Stimulated Emission of Radiation*. The first operating laser was set up by Theodore Maiman in 1960, using Al_2O_3 doped with Cr^{3+} (ruby) as the gain medium.[30] There are three possible interaction processes between light and matter as shown in Figure 2: 1) Absorption, where one incident photon imparts its energy to an electron, exciting it to a higher energy level. 2) Spontaneous emission, in which an electron in an elevated energy state relaxes spontaneously to a lower energy state and the loss of potential energy results in the emission of a photon with the same energy as the difference between the energy levels. The likelihood of spontaneous emission is controlled by the electronic transition probability. 3) Stimulated emission, which only occurs under the influence of an external electromagnetic wave. An incoming photon with energy $h\nu$ passes by an electron in an excited energy state, and stimulates the emission of a twin photon. This twin photon has the same energy, same direction, same polarization state, and same phase as the original inducing photon. Thus, the interaction between a photon and an excited atom results in two identical photons, a net amplification. The exact mechanism of stimulated emission is not fully understood and continues to be debated.[31]

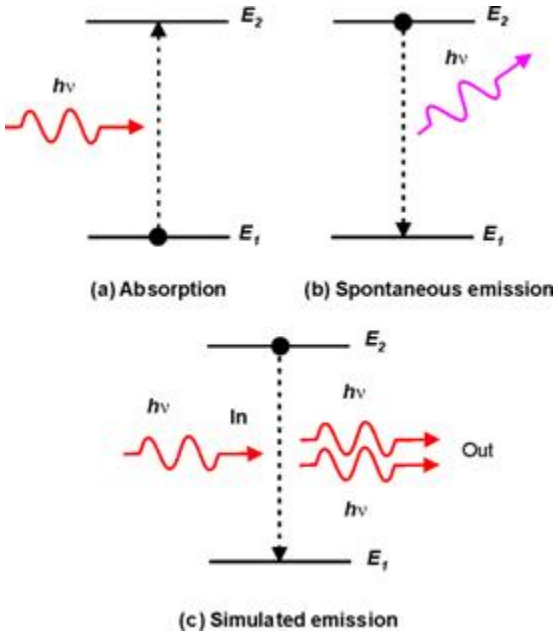

Figure 2. Absorption and emission processes in a two level electronic system.[32]

a. Continuous Wave vs. Mode-locked Lasers

When a laser is continuously being pumped and continuously emits light, it is operating in continuous wave (CW) mode. Single frequency emission can occur in a single resonator mode, or multiple modes can be emitted. In CW operating mode, the amplitude and frequency of the electromagnetic waves remains a constant with time.

A mode-locked laser is one to which either active or passive mode-locking has been applied to cause it to emit a periodic train of ultra-short pulses.

Figure 3 shows the single frequency emission mode of the Ti:Sapphire crystal while pumped by a 532 nm beam in the XL 500 laser that was used in this work. As shown in Figure 3, ultrashort pulses have a broad bandwidth, requiring the gain medium used in a mode-locked laser to have a large gain bandwidth.

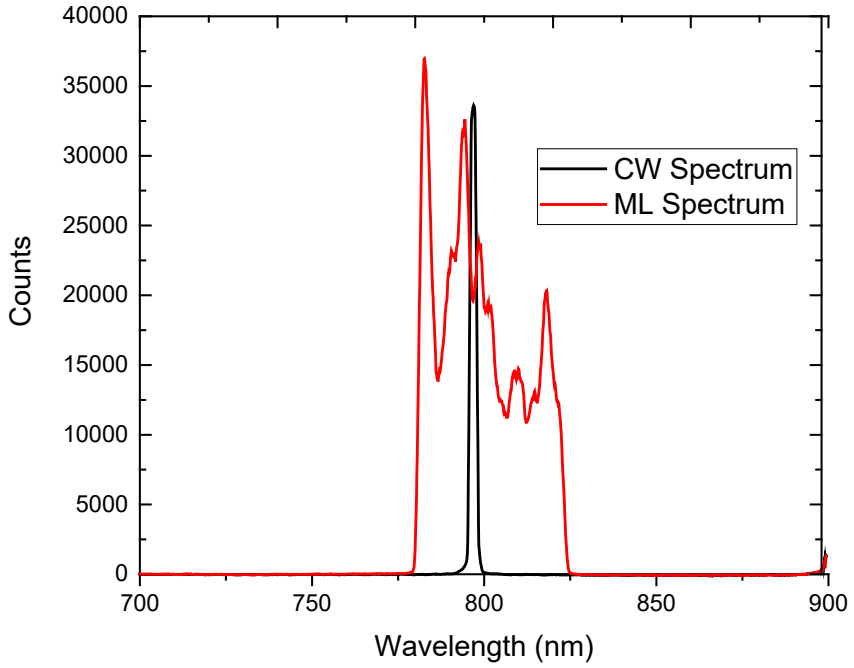

Figure 3. Spectrum of the XL 500 Laser operating in continuous wave mode and mode locked mode.

II. Background on Fs Pulse Lasers

Ultrashort timescale laser pulses are one of the more recent developments in the field of stimulated laser emission. The first Ti:Sapphire oscillator was built in 1982 by Peter Moulton at the Lincoln Laboratory[33]. In the fs pulse laser used in this thesis, a 532 nm green pump laser is used to stimulate emission in a titanium doped sapphire crystal (Ti:sapphire). The wavelength of the pump beam was chosen because 532 nm corresponds to the highest absorption bandwidth for Ti:sapphire. When the Ti:sapphire crystal absorbs the 532nm beam, the Ti atoms are excited in the lattice by 1.5 eV. When the atoms relax back to the ground state energy, they emit photons containing energies of 1.5 eV, corresponding to 800 nm wavelength according to the equation:

$$E = h\nu \tag{1}$$

where h is Planck's constant and ν is the frequency of the light.

Each excited Ti atom emits photons that can travel in any direction, but as the pump beam passes through the Ti:sapphire, it linearly excites atoms along the beam path, which give off photons which constructively interfere with each other in the direction of the beam propagation, resulting in maximum gain occurring in this direction. The Ti:sapphire crystal is placed within an oscillation cavity that consists of two end mirrors, and multiple mirrors within the cavity to direct the beam and elongate the path that the beam travels between the end mirrors. As the waves of light reflect between the end mirrors and pass repeatedly through the Ti:sapphire crystal, more atoms are excited and more photons are emitted in what is known as laser gain. If the gain exceeds the losses of the system, the intensity of the light increases and "lasing" occurs.

The distinguishing feature of a fs pulse laser is the capability to be mode-locked. Mode-locking is achieved when a phase relationship between the modes in the oscillator cavity is fixed such that the phases constructively or destructively interfere at different points in time. This creates a standing wave or longitudinal mode in the oscillator cavity that results in a pulse train of stimulated laser emission with pulse durations in the fs scale. For the pulse to have short time duration, it must contain a broad range of frequencies, these frequencies are produced by the Ti:Sapphire gain medium.

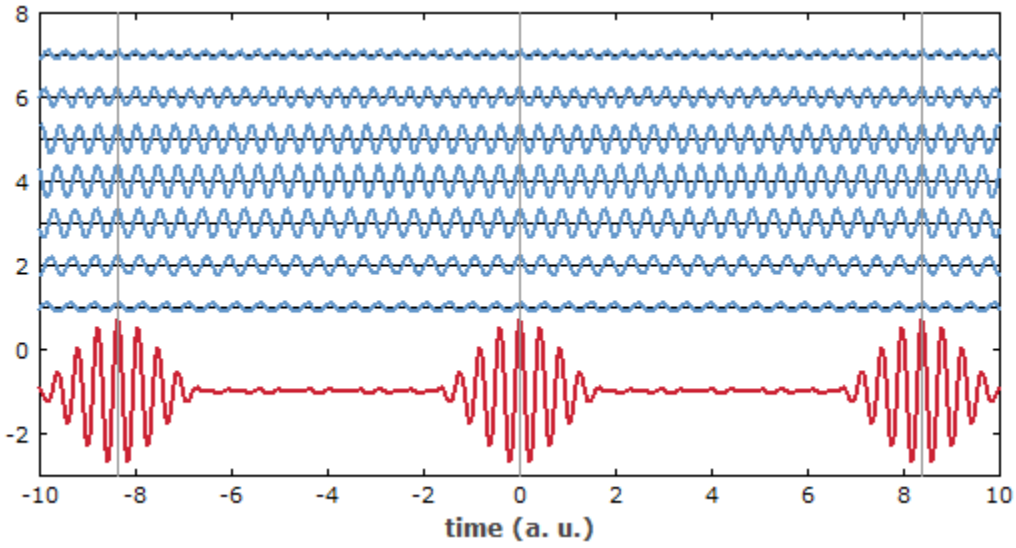

Figure 4. Synthesis of a periodic pulse train (red curve) by adding seven oscillations with slightly different frequencies (blue curves). The vertical lines indicate points in time where all the oscillations add up in phase.[34]

When lasing occurs, all of modes necessary for mode-locking are present within the laser beam, but are convoluted with other phases of light. To allow mode-locking of the laser, one of the end mirrors enclosing the oscillator cavity is made of a semiconducting material that makes it a Saturable Bragg Reflector, or SBR. Under normal conditions the SBR has a reflectivity of approximately 70%, but under increased intensity the reflectivity of the mirror increases up to 90%. By quickly shifting the location of the mirror next to the SBR, a pulse is introduced into the oscillator cavity, which briefly increases the intensity of light incident to the SBR. Because the reflectivity of the SBR is briefly increased, this pulse is then preferentially reflected and begins to oscillate in the cavity and continuously excites the Ti:sapphire crystal, resulting in a regularly repeating train of optical pulses. The Ti:sapphire crystal is still continuously pumped by the 532 nm green beam to compensate for energy loss in the system, but as the oscillating pulses continue to grow in energy through constructive interference, the continuous wavelength emission is eliminated through destructive interference. Within the oscillator cavity the pulse duration is on the order of 500 fs, this pulse is compressed in space and time through the use of dispersive optics to result in a pulse lasting under 50 fs for use in experiments.

III. Prism Compression

The final interaction of the laser beam with the oscillator cavity occurs at the output coupler. The output coupler is a partially reflective mirror that reflects part of the incoming beam and allows the remainder to transmit through. After passing through the output coupler the beam enters the prism compression unit. Each pulse of laser light is composed of broadband wavelengths centered about 800 nm. This variation in wavelengths allows for the pulse to be shortened in time using the dispersion effects of prisms. Two prisms are placed at an angle to one another such that the beam passes through them, net negative dispersion takes place and the pulse duration is shortened.

IV. Short Pulse Laser Ablation

One important function of fs pulse lasers is the ability to remove or ablate material, allowing them to be used for thin film deposition; for micromachining device structures; for the modification of material properties; and for precisely restoring and cleaning works of art.[35] Fs pulse laser ablation has been increasingly used to create structures and modify

surfaces in metals, dielectrics, and biomedical applications.[28,35,36] Fs pulse micromachining offers several unique advantages compared with ablation using longer pulses and continuous wave lasers. Damage induced in the material is confined to the focal volume of the laser due to the nonlinear nature of the absorption process.[29] High structural accuracy and a small heat affected zone are best achieved by micromachining near ablation threshold conditions.[28]

V. Physical Ablation Mechanisms

Short pulse lasers interact with materials differently than long pulse lasers. For pulse durations longer than several tens of picoseconds, laser excited electrons transfer a large amount of energy to the lattice on the same timescale as the laser pulse. Energy deposited in the focal volume of the laser is dissipated by thermal diffusion. The irradiated material is damaged when the temperature in the focal volume becomes sufficient to melt or fracture the material. The laser pulse deposits energy into the material and thermal diffusion transports it out of the irradiated region, so the relative rate of energy deposition and thermal diffusion determines the damage threshold.

Ultrashort laser pulses focused into a very small area result in very high intensities, which can create the electric field strength required to cause ionization. As shown in Figure 5, several phenomena take place when a transparent material is ablated by a fs laser pulse. At the beginning of the pulse interactions, within the first 10 to 100 fs energy is transferred to the material by nonlinear photoionization mechanisms. Between 10 fs and 10 picosecond (ps), the free electron density increases to the critical value through impact and avalanche ionization mechanisms. Some of this electron energy is transferred to the lattice by carrier-phonon scattering. Once the critical density of free electrons has been reached, a free electron plasma is created resulting in a shockwave propagating from 50 ps to a few ns. Thermal diffusion takes place in the picosecond timescale while resolidification then occurs from nanoseconds to microseconds after the pulse has irradiated the sample.

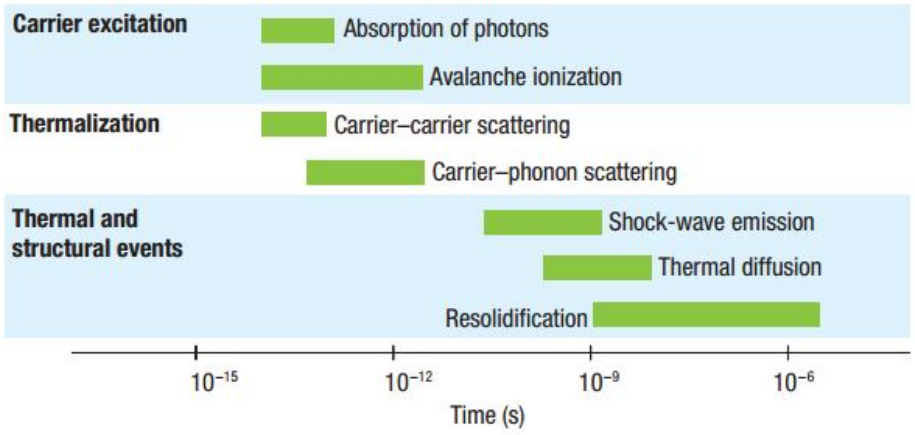

Figure 5. Timescales of processes that occur during fs pulse interaction with transparent materials. [29,37]

B. TERAHERTZ SPECTROSCOPY

I. THz Radiation

THz radiation lies between the infrared (IR) and microwave regions of the electromagnetic spectrum, and is also known as far infrared radiation. THz radiation is widely defined as covering the spectral range from 0.3 to 3 THz, corresponding to wavelengths from 1 mm to 100 μm.[38] Materials respond differently to THz radiation depending on the frequency of the radiation and the properties of the material. THz radiation is has unique sensing and imaging applications because it is easily transmitted through plastic, cloth, paper, and other dielectric materials. At THz frequencies, the permittivity of all metals is negative, making them opaque to THz radiation. THz radiation is non-ionizing and is not known to damage human tissue due to its low photon energy.

THz radiation can induce crystalline phonon vibrations, hydrogen bond stretches, torsion vibrations, low frequency bond vibrations, and rotational transitions in different materials. In solids, such as the ceramics investigated in this thesis, crystalline phonon vibrations are the primary type of response.[39] Rotational transitions are the predominant response in gases, while hydrogen bond and other low energy bond vibrations occur in liquids.

Terahertz time-domain spectroscopy (THZ-TDS)[40-42], is a relatively new characterization technique based on THz pulsed technology. Until the 1980s, a lack of efficient THz sources and detectors made THz spectroscopy a highly specialized technique that was not commonly accessible. Since then advancements in electronics and laser technology have made THz spectroscopy a popular tool for security and scientific applications. THz-TDS has been used to investigate many materials, including liquids, semiconductors and superconductors[43], explosives, and polymers[44]. THz-TDS uses pulses of radiation in the far-infrared region of the electromagnetic spectrum to probe and analyze the dielectric properties of materials. This technique uses a fs Ti:Sapphire laser to generate and detect THz radiation, based on photoconductive antennas.[45] Generally, a broadband generation of power in the frequency range of 0.06 THz – 3 THz is obtained, which is coherently detected after it passes through the sample. A fs pulse synchronized with the THz emission gates the photoconductive gap of the detector, creating a current proportional to the electric field. Measurements throughout the THz time-domain are taken by varying

the optical path length between the sample and the detector, yielding both the amplitude and phase of the incoming THz radiation, which are used to obtain the dielectric properties of materials in a noncontact and non-destructive manner.

Figure 6 shows a schematic of a THz-TDS system. The generation and detection of THz pulses is based on a femtosecond pulse laser producing a train of optical pulses. Typically a mode locked Ti:sapphire laser emitting with a center wavelength of approximately 800 nm, a repetition rate of 80 MHz and pulse durations of 100 femtoseconds is used. The femtosecond laser beam is divided into two beams, a pump beam for exciting the emitter antenna, and a probe beam for measuring the THz signal at the detection antenna. A photoconductive antenna consisting of a biased gallium arsenide chip produces THz emission when the current density, j, is modulated on a sub-picosecond timescale. Two processes create the change in current density: 1) a fs laser pulse rapidly changes the carrier density in the semiconductor and 2) an external electric field accelerates the photo-generated carriers. Detection of THz radiation is also performed using a photoconductive antenna similar to the one used for generation. A current proportional to the THz electric field is measured by gating the photoconductive gap in the antenna by a femtosecond pulse synchronized to the THz pulse. The probe beam used for characterization is passed through a delay stage that varies the optical path length travelled by the beam on its way to the detector. By varying the optical path length, the THz pulse can be sampled in the time-domain.

A typical THz-TDS measurement consists of the THz pulse being either reflected from the sample surface, or transmitted through the sample. In the case of transmission spectroscopy, used in this thesis, a sample is placed in the THz beam path, and the change in the pulse waveform is measured. Generally the amplitude of the waveform decreases after passing through the sample, and the pulse is delayed in the time domain. The transmitted waveform is compared to the reference waveform recorded with no sample in the beam and from this complex refractive index can be determined for the sample. This in turn can yield the complex dielectric constant, absorption coefficient, and conductivity. One of the main advantages of THz-TDS is the elimination of uncertainty in the determination of the phase from a Kramers-Kronig analysis.[46]

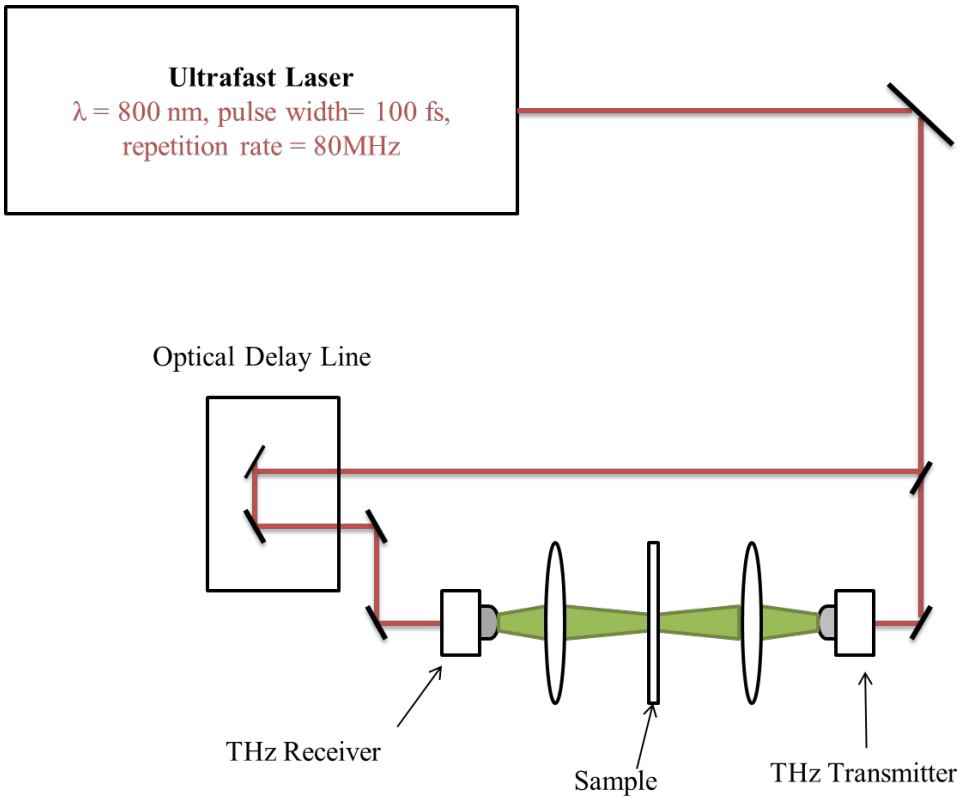

Figure 6. Schematic of a Standard THz-TDS System[47]

In the present thesis, the THz-TDS technique is used for measuring optical and dielectric properties and also the effects of processing and microstructure on these properties of single crystal and transparent ceramic YAG.

III. EXPERIMENTAL PROCEDURE

A. Sample Preparation

All samples used for investigation in this thesis were variations on the YAG structure $Y_3Al_5O_{12}$. A variety of single crystal and polycrystalline ceramic samples were used for measurements. The single crystals consisted of YAG doped with 1 atomic percent of Nd, while polycrystalline ceramics were synthesized with a range of Nd dopant concentrations. A number of samples were also acquired from Dr. Romain Gaume from the College of Optics and Photonics at the University of Central Florida. These samples were transparent ceramics formed by precisely controlling the elemental ratios of yttrium and aluminum within the garnet structure. The stoichiometric YAG composition is $Y_3Al_5O_{12}$, these samples deviated from that composition up to $Y_{3.07}Al_{4.93}O_{12.}$ Table I shows the composition of yttrium and aluminum in each of the samples.

Table I. Ratio of Yttrium and Aluminum Atoms in the Transparent YAG Samples

Sample #	**1**	**2**	**3**	**4**	**6**	**7**	**8**	**9**	**10**
Y atoms/mole	2.950	2.958	2.967	2.980	2.984	2.989	2.993	2.997	3.002
Al atoms/mole	5.050	5.042	5.033	5.020	5.016	5.011	5.007	5.003	4.998
Sample #	**11**	**12**	**13**	**14**	**15**	**16**	**17**	**18**	**19**
Y atoms/mole	3.005	3.010	3.018	3.027	3.035	3.052	3.060	3.069	3.077
Al atoms/mole	4.995	4.990	4.982	4.973	4.965	4.948	4.940	4.931	4.923

I. Transparent YAG Ceramics

A series of transparent YAG ceramics was provided by Dr. Romain Gaume of The College of Optics & Photonics (CREOL) at UCF. To prepare these samples, submicron α-Al_2O_3 and Y_2O_3 powders were mixed to produce an initial alumina rich batch. The powders were blended by wet ball milling with ethanol in a polyethylene bottle for 8 hours with 5 mm diameter dense Al_2O_3 milling media. Tetraethoxysilane (TEOS) was added to the

milling mixture by 0.5 wt% to act as a sintering aid. The ball-milled slurry was dried and the resulting powder was stored at 80 °C for one week. From this yttria-deficient mixture carefully controlled quantities were sampled, mixed, and ground with varying and also carefully controlled amounts of Y_2O_3 powder to produce 20 samples with precise compositions varying from -0.62 to + 0.96 mol % yttria below and above the $Y_3Al_5O_{12}$ garnet stoichiometry. The final powder blends were uniaxially pressed into 12.7 mm diameter pellets at 20 MPa, then cold isostatically pressed at 200 MPa. These pellets were sintered at 1750 °C in a tungsten-mesh heated vacuum furnace at under 10-6 torr, and then hot isostatically pressed at 1700 °C for 2 hours. The samples were annealed in air at 1400 °C for 3 h. To minimize the precipitation of secondary phases the cooling rates were faster than 15 °C/min. In the final preparatory step, the samples were thinned to 1 mm thickness and polished using abrasive SiC media, followed by polishing with a diamond-impregnated polymer film to achieve an optical grade surface finish. These ceramic samples were translucent to transparent in the visible spectrum with optical attenuations better than 2 cm^{-1}.

II. Opaque YAG Ceramics

a. Chemically Variant Samples

A modified combustion synthesis route was used to prepare a set of ten yttrium/aluminum solutions selected from the set of chemistries in Table I. The selected chemistries and corresponding sample numbers are shown in Table II.

Table II. Target Ratios of Yttrium and Aluminum Atoms in Opaque YAG Ceramics

Sample #	**1**	**3**	**6**	**8**	**9**
Delta%	-0.62	-0.41	-0.2	-0.09	-0.04
Y atoms/mole	2.950	2.967	2.984	2.993	2.997
Al atoms/mole	5.050	5.033	5.016	5.007	5.003
Sample #	**10**	**11**	**14**	**16**	**18**
Delta%	0.02	0.06	0.34	0.65	0.86
Y atoms/mole	3.002	3.005	3.027	3.052	3.069
Al atoms/mole	4.998	4.995	4.973	4.948	4.931

To determine the amount of metal nitrate precursor necessary to achieve the targeted atomic ratio in a 10 gm sample, calculations were worked backwards from the fully oxidized stoichiometry. From this the desired molar quantity of yttrium and aluminum atoms were calculated, and then the amount of metal nitrate necessary to yield that quantity of atoms. Yttrium nitrate hexahydrate (Acros Organics) and aluminum nitrate hexahydrate (Fisher Scientific) were dissolved one at a time in deionized water to form a clear solution. These solutions were dried for several days in a convection oven at approximately 160 °C until they formed a dense layer covered with an aerated network of dried material. This material was broken up and calcined in a Carbolite furnace with SiC elements. Each composition was calcined individually in one crucible, all with identical firing schedules. The temperature was ramped at 5 °C to 500 °C immediately followed by a ramp at 10 °C to 1000 °C where the temperature was held for 2 hours. The furnace was then turned off and cooled at a natural rate.

Following calcination, each composition was ball-milled, dry with porcelain media, in a HDPE bottle for approximately 6 hours. The milling media was separated from the powder using a 20 mesh sieve. This sieve also trapped larger particles which did not break up during milling.

The next step was to press pellets for sintering. These pellets needed to be thin enough to allow for THz-TDS measurements, but there needed to be a sufficient volume of material and associated porosity to do mercury porosimetry measurements of the pore volume distribution. Thus, for each composition, three pellets of approximately 0.7 grams were pressed, resulting in a total mass of just over 2.0 grams. Pellets were pressed in a 12.2 mm diameter die with isopropanol added to the powder to help bind it during pressing. Each pellet was pressed to 22.2 kN on a Carver press. Samples 9 and 10 both cracked when the die was pulled apart because the isopropanol created suction in the die. Dry pressing these compositions without isopropanol eliminated the cracking problem.

Since three pellets were made for each of the ten compositions, three sintering runs were performed, each with one pellet from each of the ten compositions. The pellets were arranged numerically in a rectangular high purity alumina boat, covered with a dense high purity alumina plate and fired in ambient air in a box furnace. At the beginning of each run the temperature was increased at 5°C/min. to 115°C where it remained for 2 h 15 minutes

to allow any residual water vapor to evaporate. Then the temperature was again increased at 5 °C/min. up to 1700°C for a 2 h dwell. The furnace was then turned off and the samples were allowed to cool naturally.

b. Grain Growth Study

Five pellets of YAG sample #10 ($Y_{3.0016}Al_{4.9984}O_{12}$) were pressed and fired for increasing periods of time to investigate the effects of any grain growth on the THz-TDS measurements. Each pellet was fired in ambient air atmosphere using a ramp rate of 5 °C/min. up to 1700°C. The first pellet dwelled at 1700°C for 10 min., the second for 8 h, the third for 16 h, the fourth for 24 h, and the fifth for 48 h.

B. Laser System

In this work, two laser systems were used to irradiate ceramic and single crystal YAG materials. One, a 400 mW fs pulse laser, was operated at the National Physical Laboratory in Teddington, UK. The other, a 2.5 W fs pulse laser, was operated at Alfred University. Both lasers operate under the same principles of operation. Laser pulses of approximately 40 fs duration were created using a system designed and constructed by FEMTOLASERS Produktions GmbH. The system consists of three main components: an energy pump, a solid-state laser oscillator cavity, and a prism compressor. The source of pump energy, a Sprout-G-15W from Lighthouse Photonics Inc., is a diode-pumped solid-state laser operating in continuous-wave mode. The laser gain medium is Neodymium-doped Yttrium Orthovanadate ($Nd:YVO_4$) which emits at 1064 nm. The laser output is converted to 532 nm by intra-cavity frequency-doubling. This pump provides a continuous beam of green light to the oscillator host material, a sapphire crystal (Al_2O_3) doped with Titanium (Ti^{3+}) atoms (Ti:S or Ti:Sapphire). Absorption of the 532 nm pump beam creates the required population inversion in the Ti:Sapphire crystal to result in stimulated emission.

I. Laser Irradiation

Two 1 atomic % Nd- doped YAG single crystal samples were purchased from Scientific Materials Corporation (Bozeman, MT, USA) for our measurements. Both samples were cylindrical disks with diameters of 10 mm; one had a thickness of 1 mm

while the other had a thickness of 2 mm. These transparent disks were exposed to fs pulse lasers at different energies and for different time durations to observe the interaction between the short laser pulse and the materials with differing dopant chemistries. In addition, opaque YAG ceramics of the same chemical composition as the transparent ceramics were irradiated, to examine the effect of differing microstructures on the interaction between the laser pulse and material.

a. Power Calculations

Each laser pulse contains a consistent quantity of energy, but without advanced electronics, it is not possible to directly measure the pulse energy due to the short timescales involved. Instead, the average power of the beam is measured using a thermopile detector and divided by the pulse repetition rate to calculate the pulse energy. Consider a regularly repeating train of optical pulses with repetition rate $f = 1/T$ as shown in Figure 7.

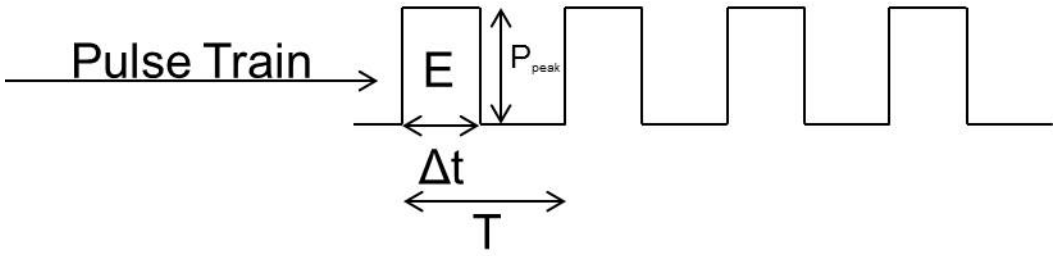

Figure 7. Regularly repeating train of optical pulses.

Assuming that the energy, E, contained in each pulse is a constant, and based on the definition of power as the rate of change of the energy flow (energy per unit time), we are led to consider two types of power. Peak power, the rate of energy flow in every pulse, is defined as:

$$P_{peak} = \frac{E}{\Delta t} \tag{2}$$

Average power, the rate of energy flow averaged over one full period, T, is defined as:

$$P_{avg} = \frac{E}{T} = Ef \tag{3}$$

If equations (2) and (3) are solved for *E* and set equal to each other,

$$P_{peak}\Delta t = P_{avg}T \tag{4}$$

Rearranging variables allows a new quantity called Duty Cycle to be defined, the fraction of time the laser is on during any period

$$\text{Duty Cycle} = \frac{\Delta t}{T} = \frac{P_{avg}}{P_{peak}} \tag{5}$$

Thus, if the average power is measured, and the Duty Cycle is known, the peak power can be calculated as follows[48]:

$$P_{peak} = \frac{P_{avg}}{\text{Duty Cycle}} \tag{6}$$

b. Fluence Calculations

To calculate the fluence and intensity of power density of the laser beam incident on the sample surface, it was first necessary to calculate the beam divergence from the beam quality factor, or M^2 factor specified for the laser system.[49] Figure 8 shows the case where the laser beam is focused to a small spot. Here the laser beam has a radius y_1, divergence θ_1, and lens focal length f. From Figure 8,

$$\theta_2 = y_1/f \tag{7}$$

From the optical invariant:

$$y_2 = \theta_1 f \tag{8}$$

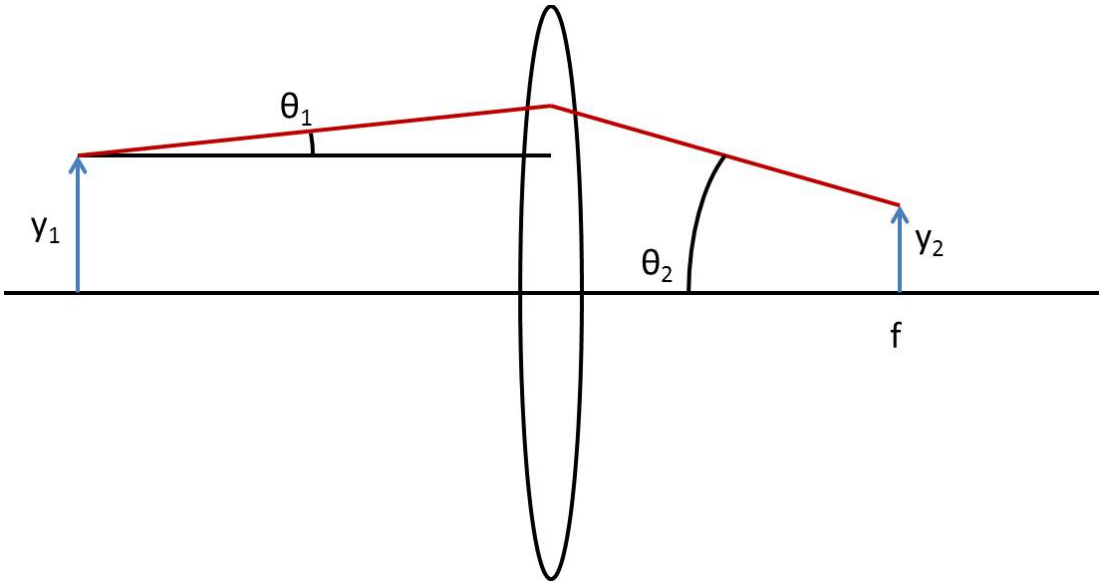

Figure 8. Schematic image showing angles, beam radii, and focal length used for spot size calculation.

The half angle beam divergence, θ_1, is defined as:

$$\theta = M^2 * \frac{\lambda}{\pi \omega_o} \tag{9}$$

where M^2 is the beam quality factor, λ is the wavelength of the beam, and ω_o is the beam radius at the beam waist.

For the 400 mW laser, M^2 was specified as 1.3, the wavelength was 800 nm, and the beam radius y_1 was 2.5 mm. These values yielded a half angle beam divergence of θ_1 = 0.132 milliradian. Therefore by rearranging equations (7) and (8), and using the lens focal length of 25 mm, the diffraction limited beam diameter at the focal point was calculated to be 6.6 μm. For the Femtolaser XL 500, M^2 was specified as 1.3, the wavelength was 800 nm, and the beam radius y_1 was 2.5 mm. These values yielded a half angle beam divergence of θ_1 = 0.132 milliradian. Therefore by rearranging equations (7) and (8) and using the lens focal length of 100 mm, the diffraction limited beam diameter at the focal point was calculated to be 26.4 μm. Figure 9 shows the focal point intensity of the 500 XL laser beam focused by a plano-convex lens as a function of the focal length of the lens used.

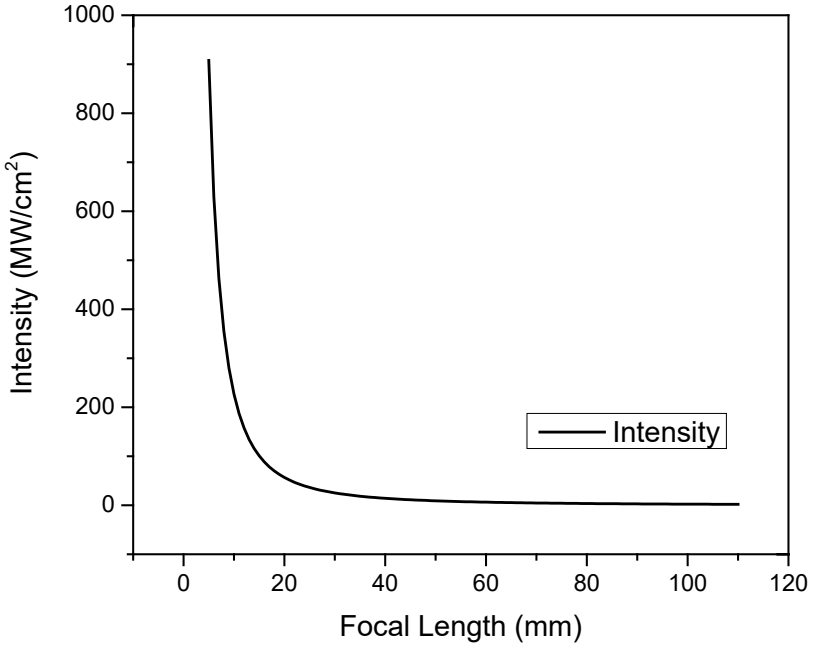

Figure 9. Laser beam intensity at the focal point as a function of the focal length of the lens used.

1. Irradiation at National Physical Laboratory

The 2 mm thick 1 atomic % Nd:YAG single crystal was sent to the National Physical Laboratory in Teddington, UK, for a laser irradiation experiment. The laser system was a Ti:sapphire fs pulse laser operating with an average power of 400 mW, an 80 MHz repetition rate, pulse duration of less than 20 fs, and a peak power of 250 KW. The relevant specifications for this laser system as well as the system operated at Alfred are given in Table III. A plano-convex lens with a focal length of 25 mm was used to expose the sample to laser radiation in six different locations, each for a different period of time. The time durations of exposure were 10, 20, 50 100, 200, and 500 seconds, as shown in Figure 11.

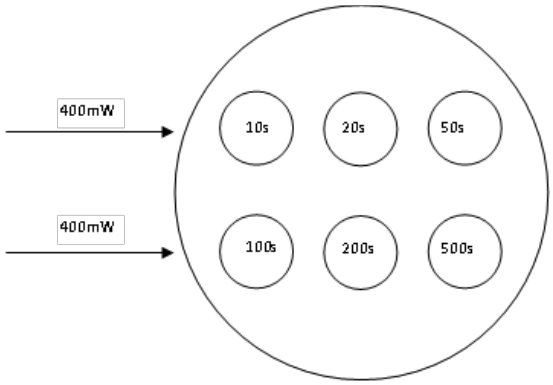

Figure 10. Schematic showing the different times of exposure on the 1 atomic % Nd:YAG transparent disk.

Table III. Specifications for the Two Laser Systems Used to Irradiate Samples

Average Power	400 mW	2.5 W
Repetition Rate	80 MHz	5.1 MHz
Pulse Duration	<20 fs	<50 fs
Pulse Energy	~5 nJ	~500 nJ
Peak Power	250 KW	10 MW
Wavelength	800 nm	800 nm

2. Irradiation with Alfred Laser System

A FEMTOLASER XL 500 fs pulse laser was used to expose various yttrium aluminum garnet samples, ceramic and single crystal, transparent and opaque, doped and undoped. The optical layout for the XL 500 system is shown in Figure 11. The laser cavity is shown in Figure 12. Note the 532 nm pump beam located on the right hand side of the image, compared to the 800 nm beam invisible to the naked eye passing through the prism compressor located on the left hand side. The samples were secured to a Thorlabs XYZ translation stage to allow the sample position to be adjusted in relation to the beam. The

flat sample surface was oriented perpendicular to the incoming beam, which was focused using a 100 mm focal length BK7 plano-convex lens.

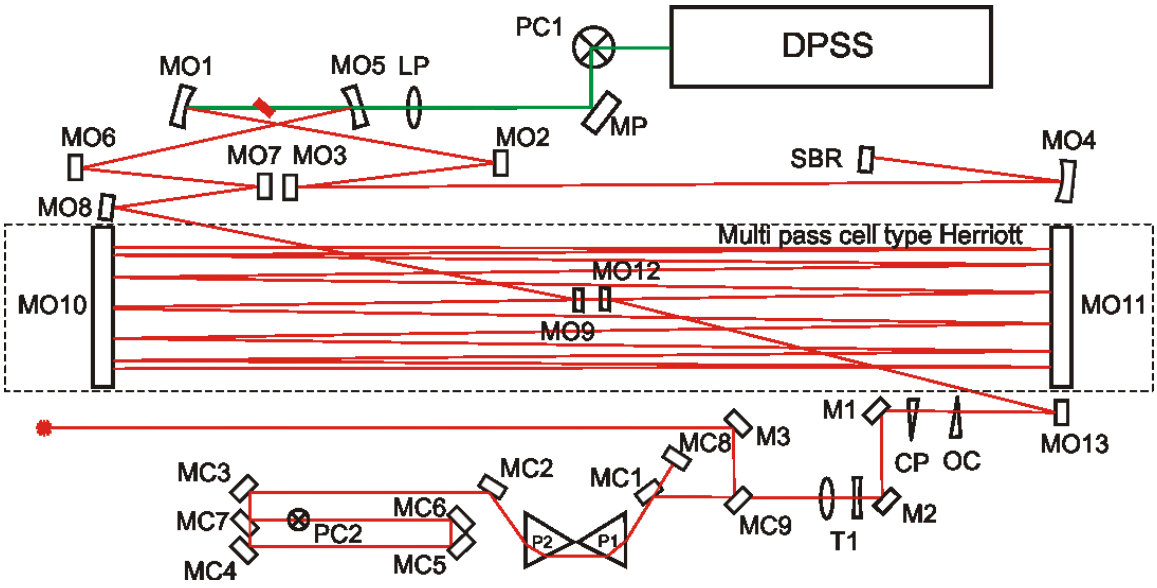

Figure 11. Optical layout for XL 500 system. A diode pumped solid state laser (DPSS) is used as the pump source for the fs laser. The short arm of the oscillator cavity consists of the path from MO1 to the SBR, while the long arm of the cavity is made up of all the mirrors from MO5 to the output coupler (OC). The multi pass Herriott cell greatly increases the effective path length of the long arm.

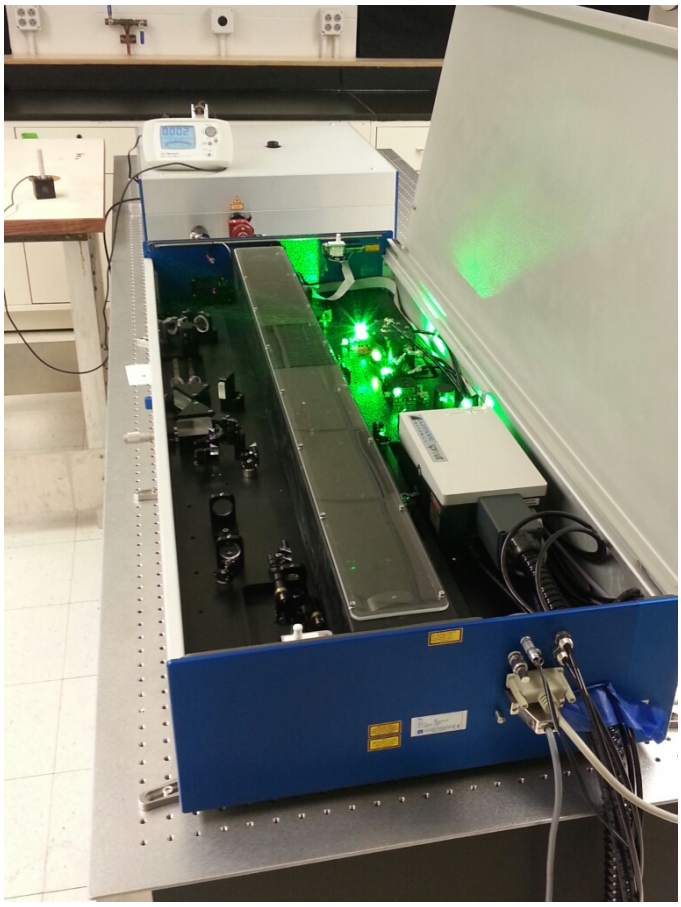

Figure 12. FEMTOLASER XL 500 system in operation. Observe the green 532 nm pump beam and the bright light emitted by the Ti:Sapphire crystal.

Figure 13 shows a CCD camera image taken to show the beam shape. The image was taken with the laser in CW mode to prevent damage to the silicon chip in the CCD camera. Several reflective neutral density filters were used to decrease the intensity below the saturation limit of the camera, multiple reflections between the various filters resulted in the fringes seen in the image.

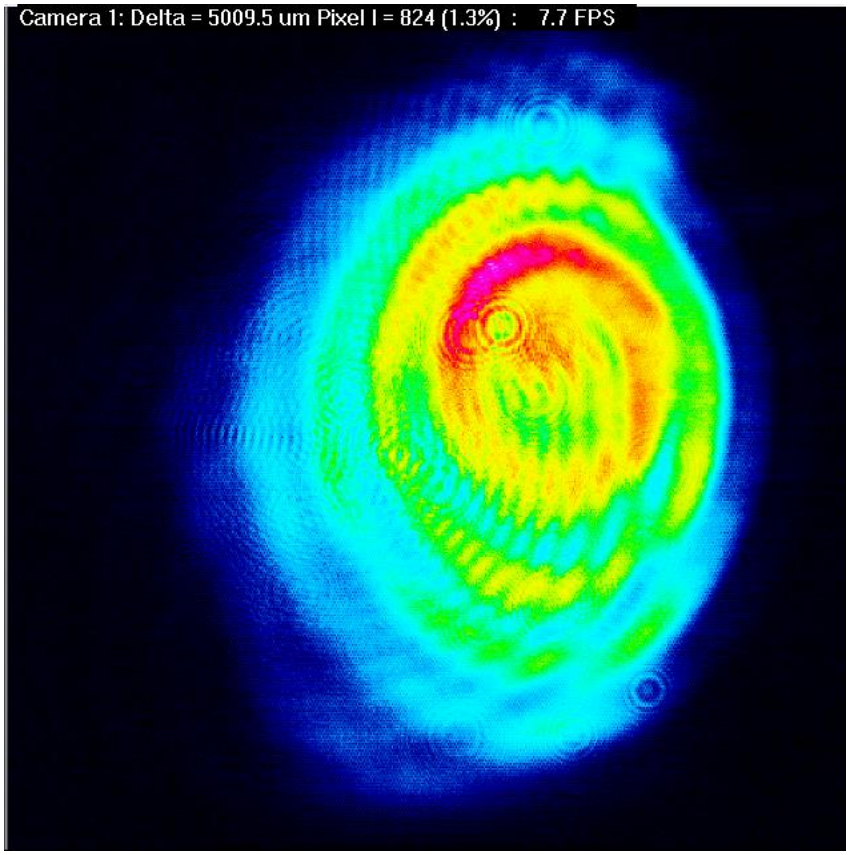

Figure 13. Cross-sectional CCD camera image of continuous wavelength laser beam showing the cross-sectional intensity.

The sample was placed with its surface aligned concentrically with the laser beam path, and was moved longitudinally in and out of the beam waist at the focal length of the lens. A number of apertures were placed along the beam path to block its propagation, and these were all opened with the sample placed about 3.0 cm beyond the focal length. The sample was moved in 0.25 cm increments longitudinally back towards the focal length, while the output spectrum of the laser was monitored with a spectrometer. The laser spectrum indicated that the laser was mode-locked and operating in pulsed, rather than CW mode. When the sample was moved to within approximately 0.30 cm of the focal length, the laser spectrum abruptly changed to CW mode, likewise, with the sample situated inside the focal length of the lens and moved outward into the focal length, at a distance of 0.30 cm from the focal length the spectrum changed to CW. This was taken to indicate that the tightly focused beam reflected perpendicularly from the sample surface and propagated back into the oscillator cavity, destructively interfering with the pulses oscillating in the

resonant cavity, destroying the mode-lock. To eliminate this problem a sample holder was fabricated to orient the sample at a 45-degree angle rotated about the vertical axis relative to the incoming beam. This allowed the beam reflected from the sample surface to be directed to a beam dump, rather than back into the laser oscillator cavity.

With the sample placed at a 45° angle relative to the laser beam, it became impossible to raster the beam across the sample surface without changing the focus on the surface, so a Faraday interferometer was placed in the beam path to prevent reflections back into the laser source and the remainder of sample exposures were carried out with the surface perpendicular to the incident laser beam.

Using the software motion control of the XYZ sample stage, the sample was moved perpendicular to the laser beam at different velocities so that linear patterns were scanned across the surface of the sample. The sample was scanned at 0.1 mm/s, 0.25 mm/s, 0.5 mm/s, 1.0 mm/s, 1.5 mm/s, and 2.0 mm/s.

C. Characterization of material properties

I. Light Scattering Particle Size Analysis

A HORIBA LA-910 Laser Scattering Particle Size Distribution Analyzer (Irvine, CA, USA) was used to characterize the size of the YAG powders prior to pressing and sintering. In this system, light irradiating the particles scattered at various angles. Large particles caused scattering concentrated in the forward direction, while small particles scattered in all directions. Thus, to measure small particles data must be collected over large angles, while to measure large particles data must be collected on the scattered light intensity at small angles.

To measure the distribution of small-angle scattered light for large particle measurement, a condenser lens was used to condense the light on a ring-type detector. For small particle measurement, detectors were located at the side and rear to measure the large-angle scattered light intensity. From the angular distribution of the scattered light intensity, the Mie scattering theory was used to calculate the particle-size distribution. Three measurements were performed for each sample, and the results were averaged together.

II. THz-TDS

Two sets of measurements were made for the transparent, chemically varied YAG ceramic samples using a Teraview TPS 3000 THz-TDS system. All samples were characterized using a THz-TDS (TPS Spectra 3000, Teraview, Cambridge, UK), which has an 8-F configuration and a useable bandwidth extending from 0.06 to 4 THz.

a. Standard measurements at room temperature

Time domain spectra were collected for each of the 18 samples at room temperature. Five identical measurements were performed on each sample, with the circular sample rotated approximately 60° between each measurement, for a total rotation of 360°. The results of each measurement were then averaged to account for any effect of inhomogeneity within the sample on the results. This set of measurements was performed twice, days apart, to check the reproducibility of the results. The results were consistent, and were combined as an average, and the pooled standard deviation was calculated for the combined data sets.

b. Temperature dependent measurements

The samples were attached to a mechanical holder with a 3.5-mm-diameter optical aperture, while another identical clear hole was used as a reference. Both sample and reference were centered over the 3.5 mm THz beam waist alternatively in order to ensure the entire frequency component passing through the sample and reference. The measurement chamber was purged with a 5 L/min flow of dry nitrogen until the disappearance of THz water vapor absorption lines. Absorption measurements as a function of temperature were carried out in a temperature-controlled cell in which the samples were held under vacuum. A thermal equilibration time of 1h was allowed before all measurements. The transmitted electric field of the pulses through the sample and of the reference were recorded in time domain and the corresponding frequency spectra were obtained by numerical Fourier transform.[18] Due to the limited thickness of the samples, the main transmitted terahertz pulse through the sample is trailed by multiple-reflected pulses in time domain. However, the clean separation between the main transmitted THz pulse and the first internal reflection enabled us to perform data analysis on the main pulse only. In order to increase the signal-to-noise ratio, every pulse curve was the average of five individual measurements from which the complex dielectric function and the absorbance

of the samples was deduced. The complex spectrum of the transmitted sample pulse E_s can be expressed in terms of the reference spectrum E_{ref} and the transmission as:[19]

$$E_s(\omega) = E_{ref}(\omega) t_{12} t_{21} e^{iL(k-k_0)} e^{-\alpha L/2} \quad (10)$$

where t_{12} and t_{21} are the frequency-dependent complex Fresnel transmission coefficients, L is the thickness of the sample, α is the power absorption, and $k = 2\pi n/\lambda$ and $k_0 = 2\pi/\lambda$ are the propagation wave vectors. Based on this relation, the frequency-dependent dielectric function, refractive index n(ω) and the absorbance values α(ω) of the samples can be determined.

III. X-ray Diffraction (XRD)

X-ray powder diffraction (XRD) was used to analyze the crystalline phase of the materials. A Bruker D8 ADVANCE diffractometer was used to scan from 10 to 70 degrees (2θ) with a step size of 0.025 (2θ degrees) and an integration time of 0.5 seconds. The excitation voltage was 40 kV and current 30 mA.

IV. Grazing Incidence X-ray Diffraction (GIXRD)

Due to the large penetration depth of X-ray radiation, GIXRD was used to study the surface layers of samples that had been exposed to the fs pulse laser. GIXRD is a diffraction technique utilizing small incident angles for the incoming x-ray beam to maximize the signal from the surface layers and make the measurement surface sensitive. By increasing the path length of the incident beam through the affected surface layer, the intensity from this region is increased and the diffracted intensity from the substrate is decreased to allow for phase identification restricted to the matter in the surface layer.

For these measurements, Cu (Kα) X-ray radiation was used at a constant incident angle of 2.0° with an excitation voltage of 40kV and current of 30 mA. The diffraction angle was varied at a step size of 0.04 2θ (°) with a dwell time of 15 seconds at each step.

V. Archimedes Density Measurements

The density of samples has an effect on the results of THz-TDS measurements due to the composite concentration of combining dense ceramic and air contained within the pores. Samples with densities less than their theoretical maximum value have an "effective refractive index" less than the theoretical value, which, it is hypothesized, can be accounted

for by normalizing for density. To account for slight variations in sample geometry, density measurements based on Archimedes' Principle were used as a way to measure the pore volume and model the effective thickness.[50] Three measurements were taken for the density calculation: dry mass (M_{dry}), saturated mass (M_{sat}), and suspended mass (M_{susp}). All measurements were in grams. First, the samples were dried on a hot plate at 140 °C for one hour to evaporate any residual water and the mass of each as M_{dry}. Then, the samples were immersed in deionized water and degassed in an evacuation chamber for 24 hours. After degassing excess water on the sample surface was removed by gently wiping with a lint-free paper wipe. The mass was then recorded as M_{sat}. Next the sample was immersed in deionized water in the beaker on the balance pan and the mass was recorded as M_{susp}. The temperature of the suspending medium, water, was also recorded, because the density of the suspending medium (ρ_w) is dependent on temperature. Equation shows the calculation used for determining the density of the sintered pellets (D_s).

$$D_s = \frac{M_{dry} * \rho_w}{M_{sat} - M_{susp}} \tag{11}$$

VI. Mercury Porosimetry

Pore size and volume distribution measurements were carried out using a Micromeritics Autopore 9220 Mercury Porosimeter. Mercury contact angle was 140° with a surface tension of 0.485 N/m. the equilibration time for each pressure measurement was 60 seconds.

VII. Scanning Electron Microscopy (SEM)

a. Grain Size Measurements

Environmental Scanning Electron Microscopy was used to evaluate the grain sizes of samples characterized in THz-TDS. For the transparent YAG ceramics in the stoichiometry range $Y_{2.95}Al_{5.05}O_{12}$ to $Y_{3.077}Al_{4.923}O_{12}$, samples for grain size measurements were created by cutting a circular segment from each of the cylindrical disks. Each circular segment had height of approximately 1 mm. These circular segments were arranged on a piece of platinum foil and thermally etched to reveal the grain boundaries for analysis. The samples were placed directly in a furnace operating at 740°C, and immediately the temperature was increased to 1050°C at a rate of 150°C/minute. The temperature was then increased incrementally to 1450°C at an average rate of 25°C/minute for a 30 minute dwell. SEM micrographs were recorded

using magnifications of 1000x, 1500x, and 2000x, depending on the magnification necessary to have a sufficient sample size of grains in the image for performing grain size analysis. Analysis was performed according to ASTM standard E112, using the Abrams Three-Circle circular intercept procedure. Circular test arrays automatically compensate for departures from equiaxial grain shapes, without overweighting any local portion of the field. Ambiguous intersections at ends of test lines are eliminated.51 For this procedure, a test pattern consisting of three concentric and equally spaced circles having a total circumference of 500 mm was applied successively to five blindly selected and widely spaced fields in the SEM image, and the count of grain boundary intersections with the circles was recorded. The SEM images used for this analysis are shown in the appendix. For samples 2, 3, and 4, the microstructure consisted of grains encapsulated in a matrix, which did not lend itself to the grain boundary intercept procedure. Samples 9 and 11 appeared to consist of a continuous network with poor grain boundary definition and were also unable to be analyzed. For the remainder of the samples with clearly defined grain boundaries, the ASTM grain size number G, was calculated with the corresponding average grain diameter determined using the relationship between grain size No. G and average grain diameter shown in Figure 14. The results are shown in

Table IV. In cases where the row is blank, there was not enough definition of the grain boundaries in the SEM micrograph to make an accurate analysis of the grain size.

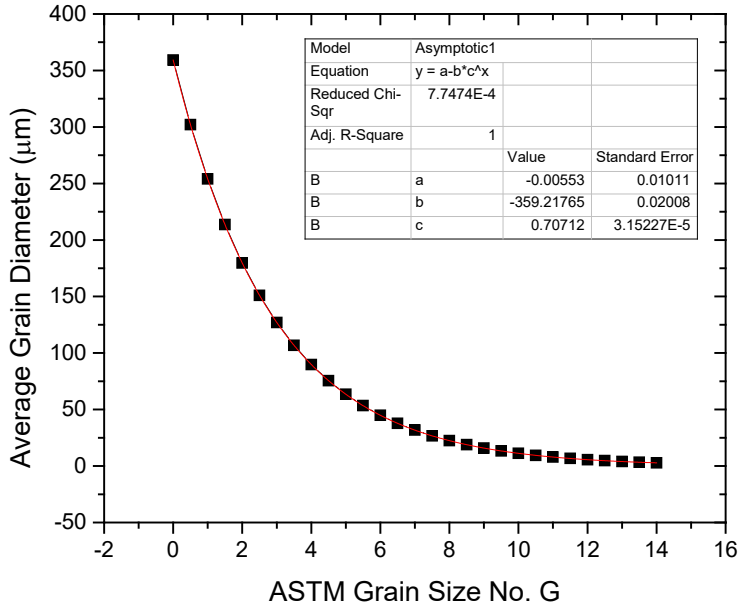

Figure 14. Curve used to calculate the average grain diameters based on the ASTM grain size number calculated using the Abrams Three-Circle circular intercept procedure.

Table IV. Chemical and Grain Size Properties of Transparent YAG Ceramics

Sample	Shift from Stoichiometry (mol %)	Chemical Formula	Grain Size No. G	Average Diameter (μm)
1	-0.62	$Y_{2.95}Al_{5.05}O_{12}$	11.05	7.8
2	-0.52	$Y_{2.958}Al_{5.042}O_{12}$	-	-
3	-0.41	$Y_{2.967}Al_{5.033}O_{12}$	-	-
4	-0.25	$Y_{2.98}Al_{5.02}O_{12}$	-	-
6	-0.2	$Y_{2.984}Al_{5.016}O_{12}$	9.92	11.5
7	-0.14	$Y_{2.989}Al_{5.011}O_{12}$	10.15	10.7
8	-0.09	$Y_{2.993}Al_{5.007}O_{12}$	10.76	8.6
9	-0.04	$Y_{2.997}Al_{5.003}O_{12}$	-	-
10	0.02	$Y_{3.002}Al_{4.998}O_{12}$	9.13	15.2
11	0.06	$Y_{3.005}Al_{4.995}O_{12}$	-	-
12	0.12	$Y_{3.01}Al_{3.99}O_{12}$	10.48	9.5
13	0.23	$Y_{3.018}Al_{4.982}O_{12}$	11.09	7.7
14	0.34	$Y_{3.027}Al_{4.973}O_{12}$	8.42	19.4
15	0.44	$Y_{3.035}Al_{4.965}O_{12}$	11.57	6.5
16	0.65	$Y_{3.052}Al_{4.948}O_{12}$	9.49	13.4
17	0.75	$Y_{3.06}Al_{4.94}O_{12}$	10.52	9.4
18	0.86	$Y_{3.069}Al_{4.931}O_{12}$	11.77	6.1
19	0.96	$Y_{3.077}Al_{4.923}O_{12}$	11.59	6.5

VIII. Wavelength Dispersive Spectroscopy (WDS)

Phase changes and elemental redistribution were investigated by collecting elemental maps using JEOL JXA-8200, WD/ED Combined Electron Probe Microanalyzer (EPMA) (JEOL Ltd., Tokyo, Japan). Elemental scans were performed at an accelerating potential of 15kV, over an area of 225×225 μm^2, step size of 0.5 μm in x- and y- directions, and a dwell time of 80 ms at each point.

IV. RESULTS AND DISCUSSION

A. Particle Size, Grain Size, Density, and Porosity Results

I. YAG Chemistry Variation Series

Figure 15 shows the particle size analysis results for the range of ceramic YAG compositions described in Table V. The error bars represent the minimum and maximum measurement values. There were some larger agglomerates, which settled out during the light scattering measurement. These represented an unknown percentage of the total powder used for sintering. SEM imaging confirmed that the small particles, which constituted these agglomerates, were on the same size order as those measured by the light scattering measurements.

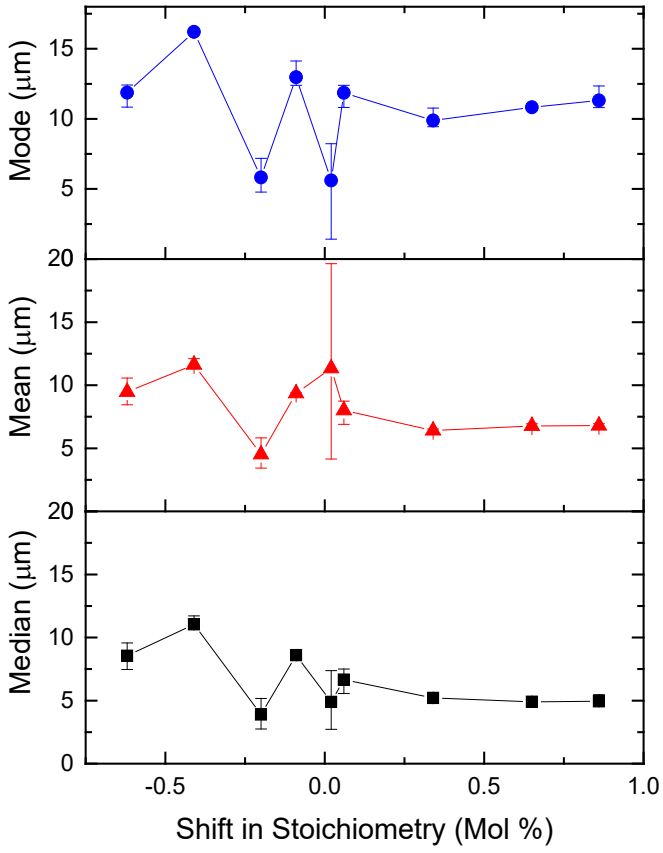

Figure 15. Median, mean, and mode of the particle size distribution measured by laser light scattering of calcined, ball-milled, but un-sintered YAG powders.

Table V. Summary Table of Opaque YAG Ceramics with Corresponding Chemical Formulas, Bulk Densities, and Average Pore Diameters

Sample #	Shift from Stoichiometry (mol %)	Chemical Formula	Density (g/cc)	Percent of Theoretical Density	Average Pore Diameter (µm)
1	-0.62	$Y_{2.95}Al_{5.05}O_{12}$	2.77	60.8	3.15
3	-0.41	$Y_{2.967}Al_{5.033}O_{12}$	2.73	60.1	2.86
6	-0.20	$Y_{2.984}Al_{5.016}O_{12}$	2.89	63.4	1.15
8	-0.09	$Y_{2.993}Al_{5.007}O_{12}$	2.75	60.4	2.77
9	-0.04	$Y_{2.997}Al_{5.003}O_{12}$	3.30	72.6	3.01
10	0.02	$Y_{3.002}Al_{4.998}O_{12}$	3.79	83.3	0.91
11	0.06	$Y_{3.005}Al_{4.995}O_{12}$	2.93	64.3	2.77
14	0.34	$Y_{3.027}Al_{4.973}O_{12}$	2.96	65.1	1.97
16	0.65	$Y_{3.052}Al_{4.948}O_{12}$	2.95	64.9	2.16
18	0.86	$Y_{3.069}Al_{4.931}O_{12}$	3.01	66.1	2.04

Figure 16 shows the microstructural features of the sintered samples. Samples rich in Al_2O_3 generally form relatively high-density agglomerates, combined into an aggregate forming a low-density pellet due to poor mass transport between agglomerates. The agglomerates are large, but made up of uniformly sized, small grains. Samples 9 and 10, which straddle the $Y_3Al_5O_{12}$ YAG equilibrium stoichiometry show the best densification, made up of uniformly sized small grains with comparatively low porosity. On the Y_2O_3 rich side, densification is low, but the small grains appears to be in the beginning stages of forming large densified regions, rather than distinct agglomerates. The size of these smaller grains is relatively consistent from sample to sample, but only the two samples closest to stoichiometry have uniform sintered microstructures. All the samples were processed as identically as possible, so the cause of the variation in microstructures is not caused by the process variations. It is most likely caused by variations in the ball-milling step that followed calcination. All the chemistries studied fall within a 1.0% +/- shift from the eutectic point of YAG, so it is not expected that the sintering behavior would be strongly influenced by the chemistry.

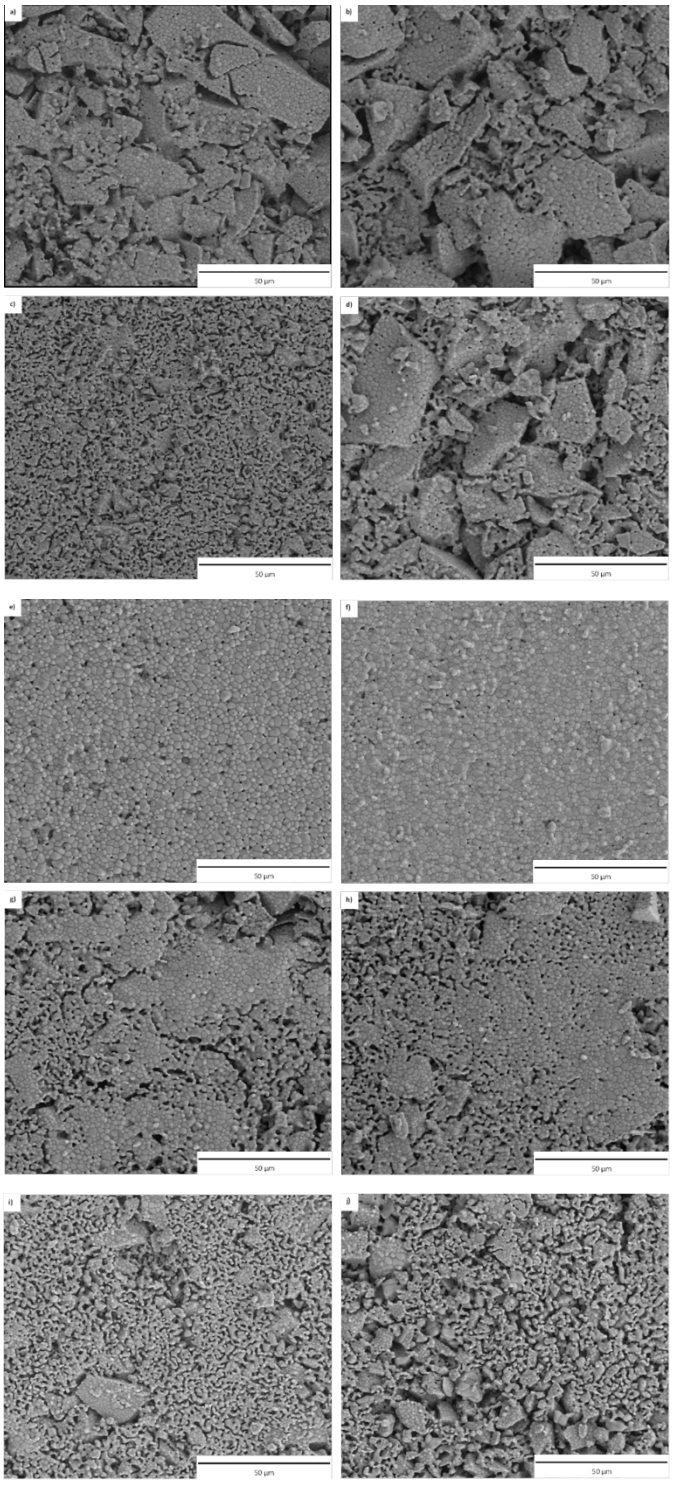

Figure 16. Microstructures of Y-Al-O pellets. **a)** # 1 **b)** # 3 **c)** # 6 **d)** # 8 **e)** # 9 **f)** # 10 **g)** # 11 **h)** # 14 **i)** #16 **j)** #18. All micrographs were taken at 1000 × magnification.

II. YAG Single Chemistry Grain Growth Study Results

Table VI shows the average grain diameter, bulk density, and percentage of theoretical density for the stoichiometric YAG pellets fired at 1700°C for varying times. The microstructures used for grain size analysis are shown in Figure 17.

Table VI. Sintering, Grain Size, and Density Information for Stoichiometric YAG Fired to Examine the Effect of Grain Size on THz Properties

Sintering Dwell Time	Average Grain Diameter (µm)	Bulk Density (g/cc)	Percent of Theoretical Density (%)
10 minutes	1.35	3.25	71.4
8 hours	2.16	3.79	83.3
16 hours	4.16	3.89	85.5
24 hours	4.63	3.78	83.1
48 hours	7.19	3.70	81.4

Three reactions take place in sequence between 900°C and 1400°C during the sintering of YAG when the starting oxides have been mixed in the correct stoichiometric proportions. The first forms the $Y_4Al_2O_9$ phase. The second corresponds to the transformation creating YAP (the $YAlO_3$ – perovskite structure). The third occurs when residual Al_2O_3 reacts with the YAP phase to form $Y_3Al_5O_{12}$ (YAG). At elevated temperatures shrinkage is due to the densification of YAG.[52] Without the use of high pressure sintering methods (*e.g.* hot pressing[53] or spark plasma sintering), it is known from literature that sintering aids such as MgO and SiO_2 are required to achieve fully dense and transparent YAG ceramics.[52]

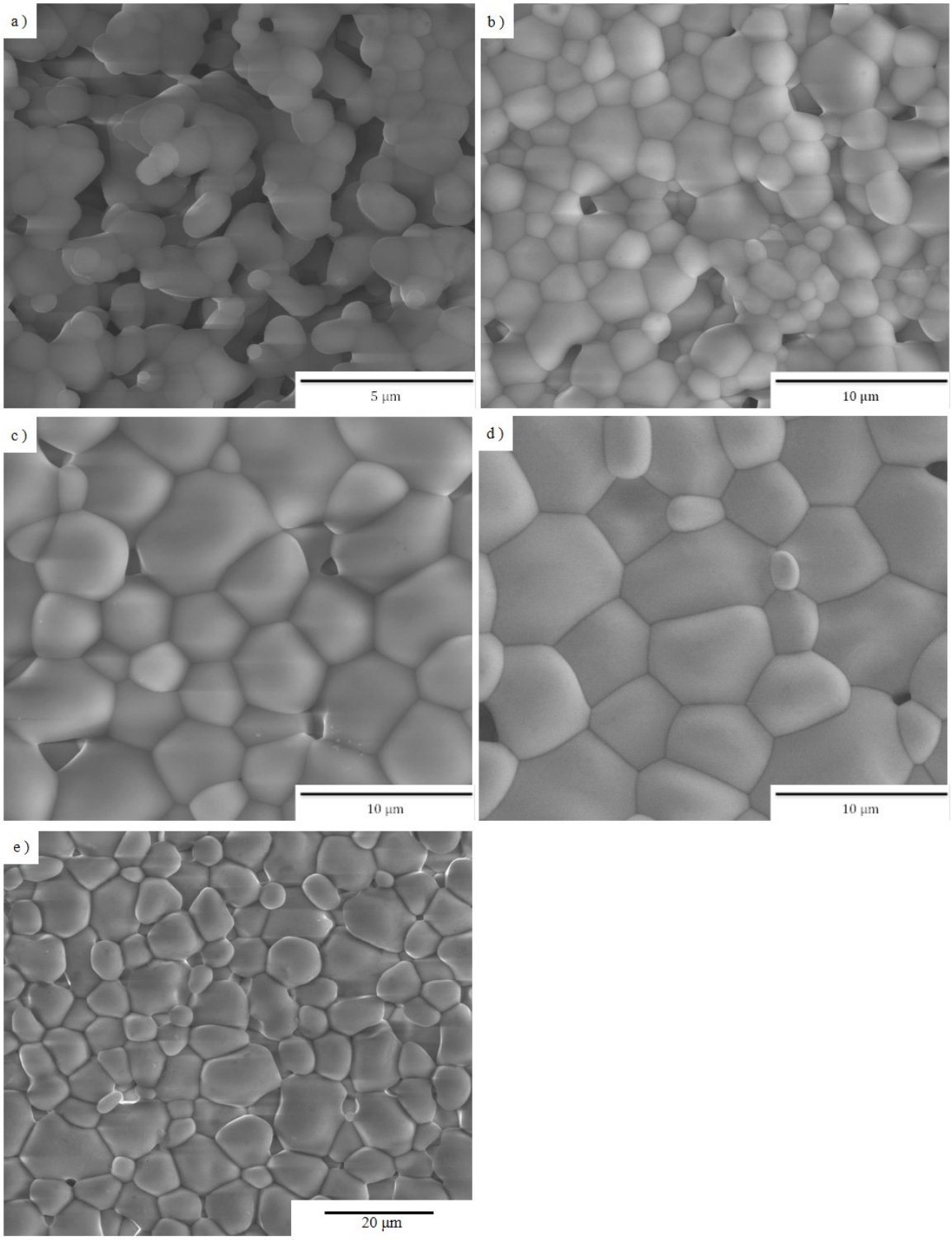

Figure 17. Microstructures of YAG ceramics fired at 1700 °C for a) 10 min, b) 8 h c) 16 h, d) 24 h, and e) 48 h.

The YAG pellet fired for 10 min exhibited the beginning stages of sintering with limited particle necking and small grains with diameters on the order of 1 µm. There was no apparent grain growth. The partially sintered grain matrix resulted in high degrees of connected bulk porosity. After 8 h of sintering at 1700°C grains had more completely bonded together, causing a reduction in porosity. Average grain diameter was around 2 µm, but with a reduction in porosity compared to the sample fired for 10 min, sintering up to 83% of theoretical density. Beyond 2 h dwell time, the sintered density plateaued at approximately 85% of theoretical density, regardless of sintering time. The 16 h dwell and the first of two 24 h dwells showed larger grains, while the second 24 h dwell had smaller grains than the first. This is due to variations in the precursor particle size. All samples were made from one precursor batch, and it is possible that variations in particle size distribution within the batch had an effect on the final grain size of these samples. The bulk density and average grain diameter are plotted as a function of sintering time in Figure 18.

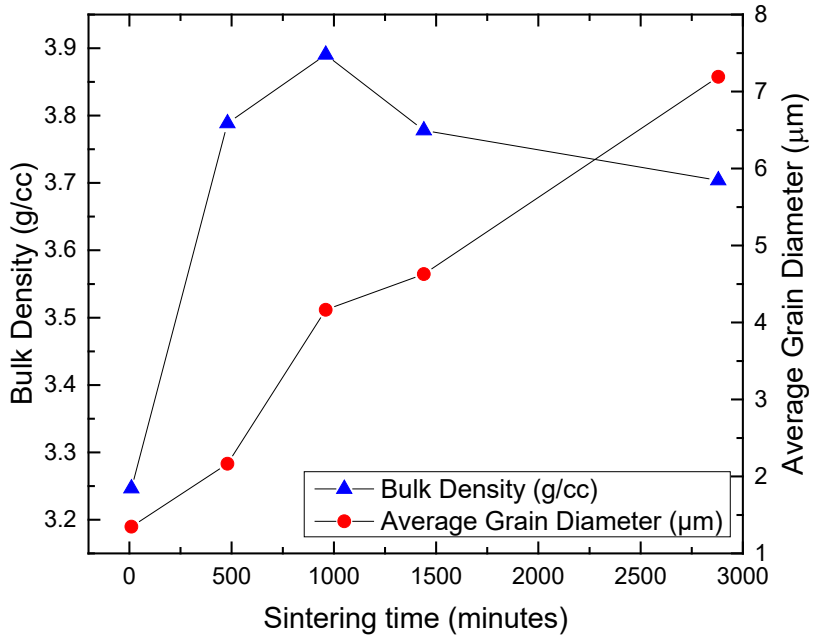

Figure 18. Bulk Density and average grain diameter as a function of sintering time at 1700°C.

B. Laser Irradiation Results (NPL)

The exposure of the 2mm thick transparent 1 atomic % Nd:YAG single crystal at NPL did not show any ablation or any other structural changes in the surface, as seen in Figure 19.

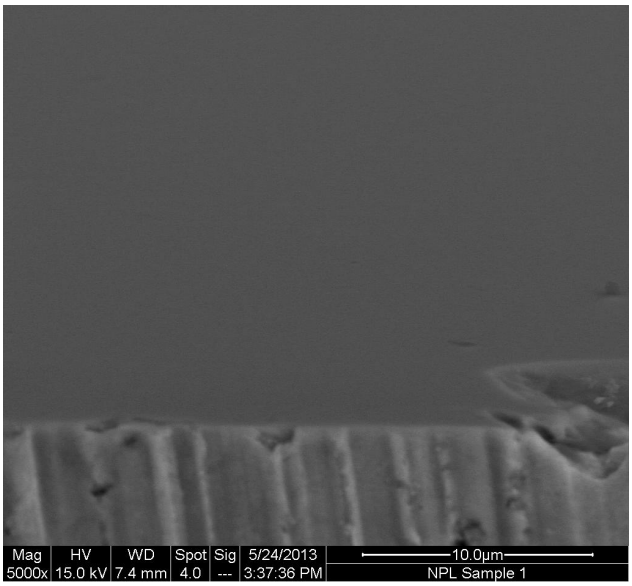

Figure 19. Representative SEM image of transparent 1 atomic % Nd:YAG exposed to focused 400 mW fs pulse laser beam. Image in SE-BSE mode.

This image showing the smooth polished surface of the disk is representative of scans taken from all over the surface of the material. No physical damage was observed. The edge of the pellet is shown as a reference point. The surface was also scanned using laser profilometry as shown in Figure 20. The polishing scratches are visible, with depths of approximately 2 µm, however over the entire surface no other features besides polishing scratches were discovered.

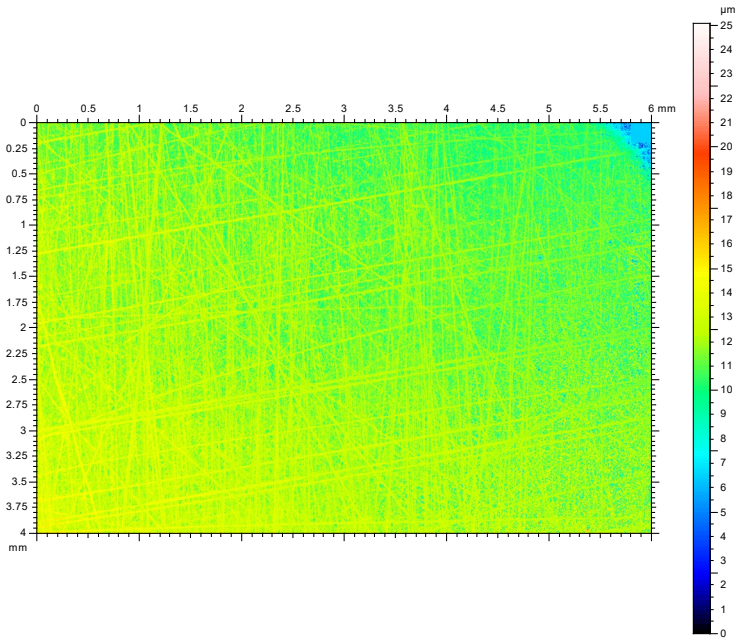

Figure 20. Laser profilometry scan of sample shown in Figure 19 reveals polishing scratches, but no ablation craters.

C. Laser Irradiation Results (Alfred University)

I. Transparent Materials

The first experiment at was performed with a 1 mm thick cylindrical disk of 1 atomic % Nd:YAG purchased from Scientific Materials Corp. The transparent pellet was moved axially along the laser beam to find the focal point where the laser fluence would be the highest. Since the focal length of the lens was known to be approximately 100 mm, the sample was placed 100 mm from the back of the lens and was alternately moved nearer to and further away from the focusing lens. Outside the focal volume of the beam, only a dull red dot was visible on the sample surface, and the transmitted red beam was visible on the screen behind the sample. As the focal point was approached, the red dot changed to a bright white spot on the sample, and the transmitted light would change from dull red to a white circle surrounded by different colors as shown in Figure 21.

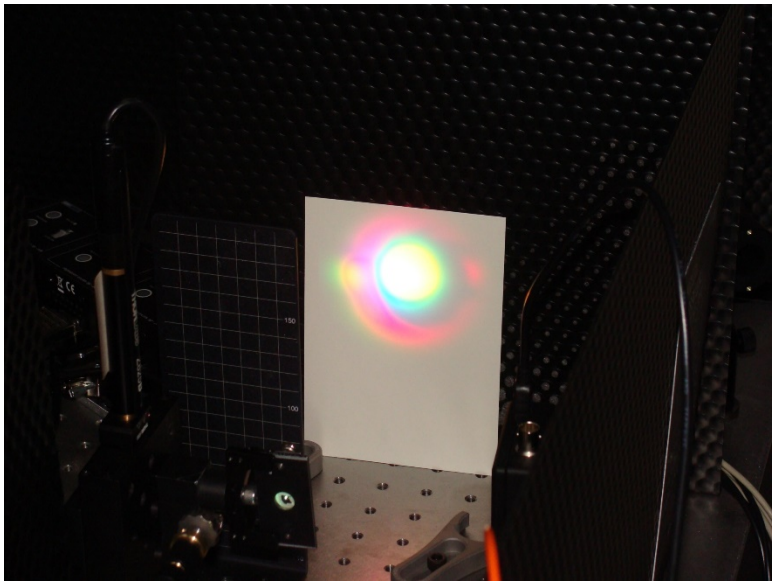

Figure 21. Colors generated by fs pulse interaction with transparent 1 atomic % Nd:YAG single crystal.

Changing the distance of the sample from the lens changed the color, as did adjusting the prism compressor to change the pulse duration. It was not possible to quantify the pulse duration with the setup at the time. Two important variables could not be quantified: the pulse duration, and the beam diameter incident to the sample surface. Assuming ideal laser operation and beam propagation, the pulse duration can be taken as 40 fs and the beam diameter at the focal point would equal 26.5 µm. The measured average laser power was 1.78 W, corresponding to a peak power of 8.7 MW. With a beam diameter of 26.5 µm the resulting peak laser intensity would be approximately 1600 GW/cm^2. However, subsequent experiments indicated that the actual beam diameter at the sample surface was 100 µm, which would result in a laser intensity of only 110 GW/cm^2 at 40 fs pulse durations. Both these values are greater than the ablation threshold of 50 GW/cm^2 reported in literature. [17] However, no ablation of the transparent material was observed.

II. Opaque Materials

a. Rastered Exposure Pattern

An opaque YAG ceramic doped with 1 atomic % Nd was exposed to the focused laser beam in a rastered pattern as shown in Figure 22. The beam was scanned continuously from left to right at a rate of 2 mm/second, then shifted up by 0.1 mm and scanned from right to left, resulting in a rectangular pattern of channels created in opposite directions. Each step in the sample stage movement was enacted manually, so at the left and right edges of the pattern a short time elapsed before the beam was shifted to the next row. This dwell explains the ablation craters that formed on the left and right edges of the image. In the center of the pattern the beam was moving continuously, so it is thought that the craters formed there may be due to sub-surface porosity or surface topography. It appears that the loose granular structure of the material has been melted by the laser beam and solidified upon cooling.

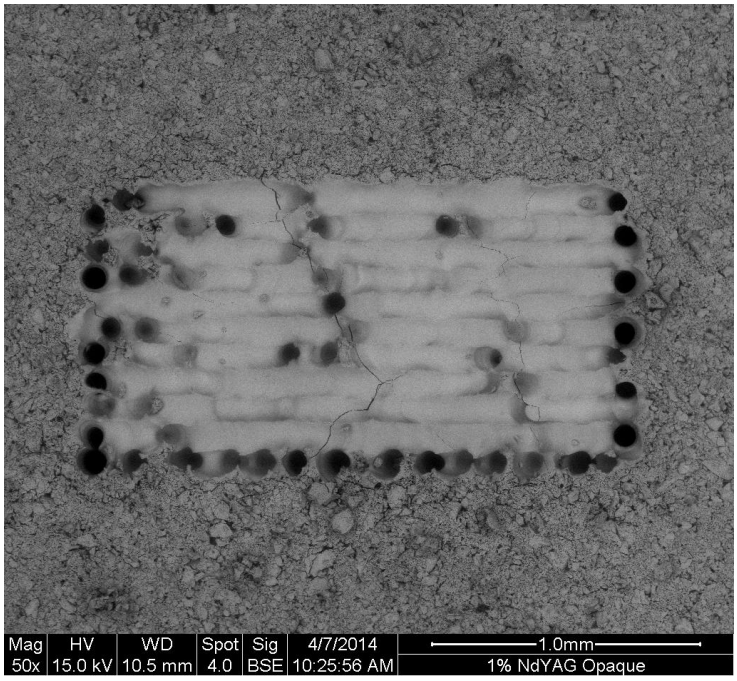

Figure 22. 50× magnification image of raster pattern of laser beam over 1 atomic % Nd:YAG ceramic. SEM image in BSE mode.

Upon further magnification and examination, the direction of the movement of the pattern can be seen alternating from row to row in Figure 23. The circular leading edge of

the laser beam is visible in the slight ridges in each line, most likely due to the resolution of the stepper motor moving the sample, which makes the motion not perfectly continuous. There are also several cracks visible, possibly due to thermal shock during rapid heating and cooling.

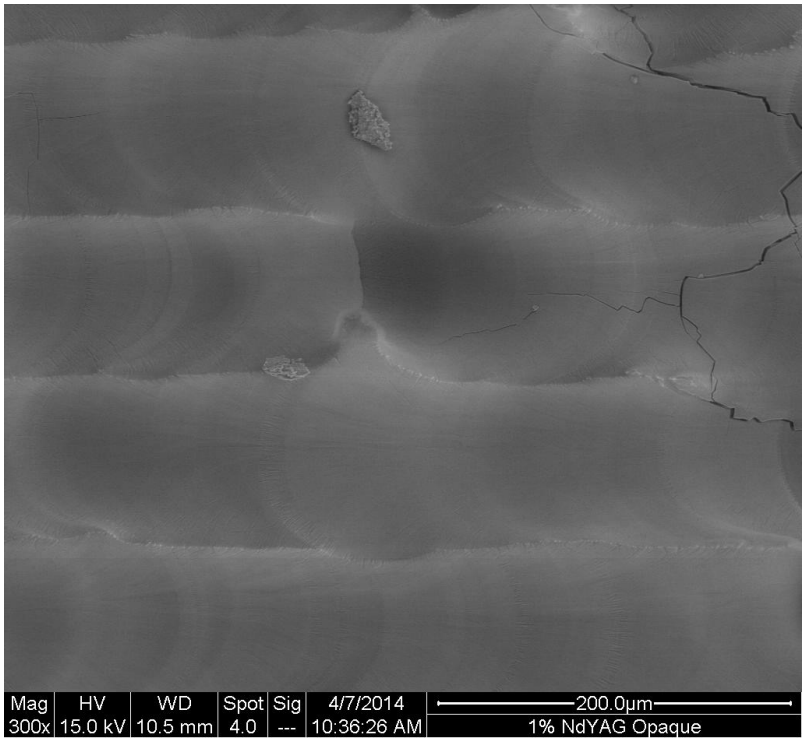

Figure 23. 300× image of laser scan pattern on 1 atomic % Nd:YAG ceramic. Note the thermal shock crack in the upper right portion of the image.

The width of the horizontal patterns in Figure 24 is approximately 100 µm. This is the expected spacing due to the 0.1 mm step size taken by the sample stage to make each horizontal pass across the laser beam. However, if the laser spot size was smaller than 100 µm we would expect to see a space of unexposed sample surface between each line. This is not the case, indicating that the laser spot size was greater than 100 µm resulting in overlap in the affected regions created by the laser energy.

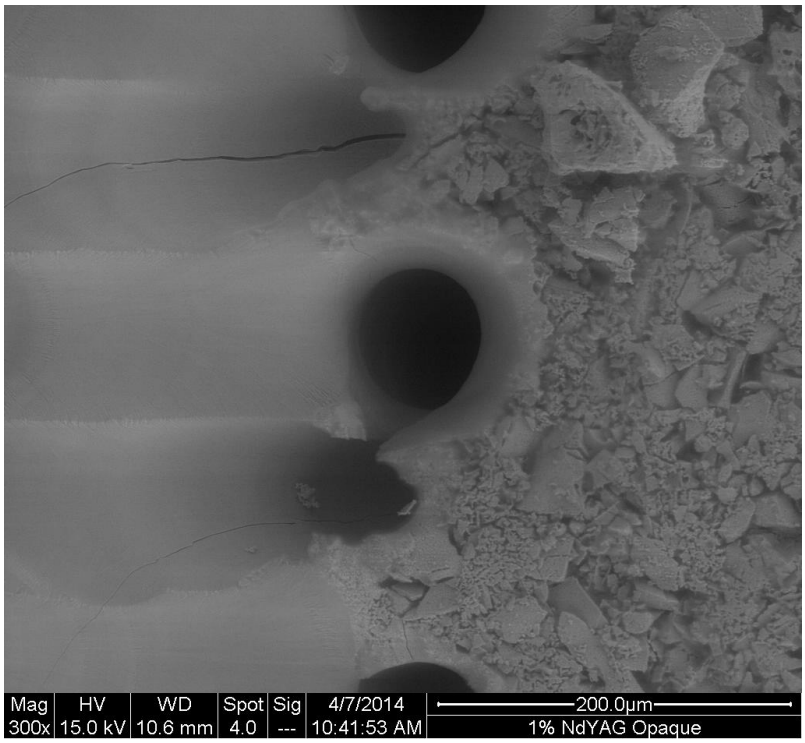

Figure 24. 300× magnification image of an ablation crater at edge of the raster pattern in Figure 22. As the direction of the sample movement changed, the beam dwelled at this point long enough to ablate a deep crater.

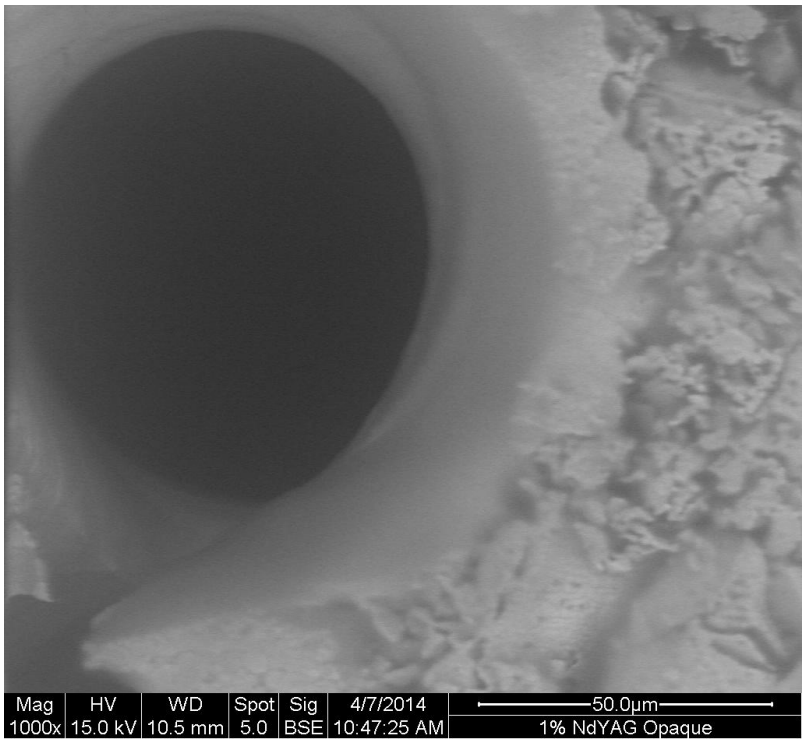

Figure 25. 1000× magnification image of the ablation crater shown in Figure 24.

By measuring the diameter of the affected region surrounding the ablation craters, it appears that the diameter of the incident laser beam was approximately 120 μm. The interior of the ablation crater, out of focus and appearing as a dark void, is approximately 80 μm. In the area surrounding the edge of the crater the affected region narrows with increasing depth into the sample. This is due to the conical shape of the focused beam.

In Figure 26, the microstructure shows that the small, approximately spherical grains of the original surface are sintered into large, thin, elongated grains with fine surface smoothness. The grains are wider at the outer edge of the beam affected area and narrow towards the center, terminating in the small grain boundaries seen in the bottom right corner of Figure 26.

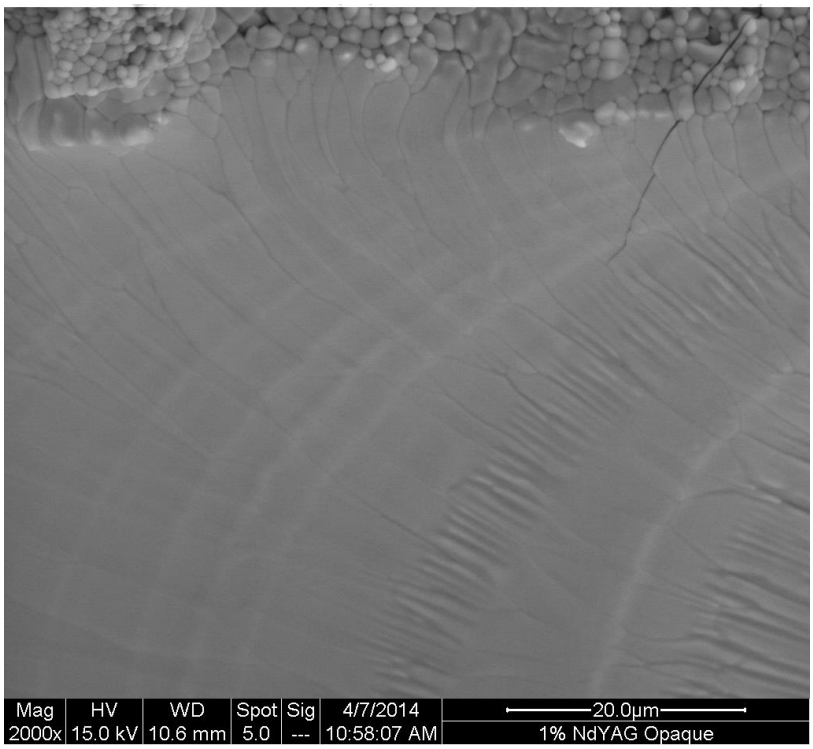

Figure 26. Image showing the transition from untreated area to area exposed to laser beam.

Wavelength Dispersive Spectroscopy

A sample of ceramic YAG #10 ($Y_{3.002}Al_{4.998}O_{12}$) exposed to focused fs pulse laser radiation was cut in cross section perpendicular to the direction of the surface channels and polished to 1 micron surface quality. The surface after laser exposure is shown in Figure 27.

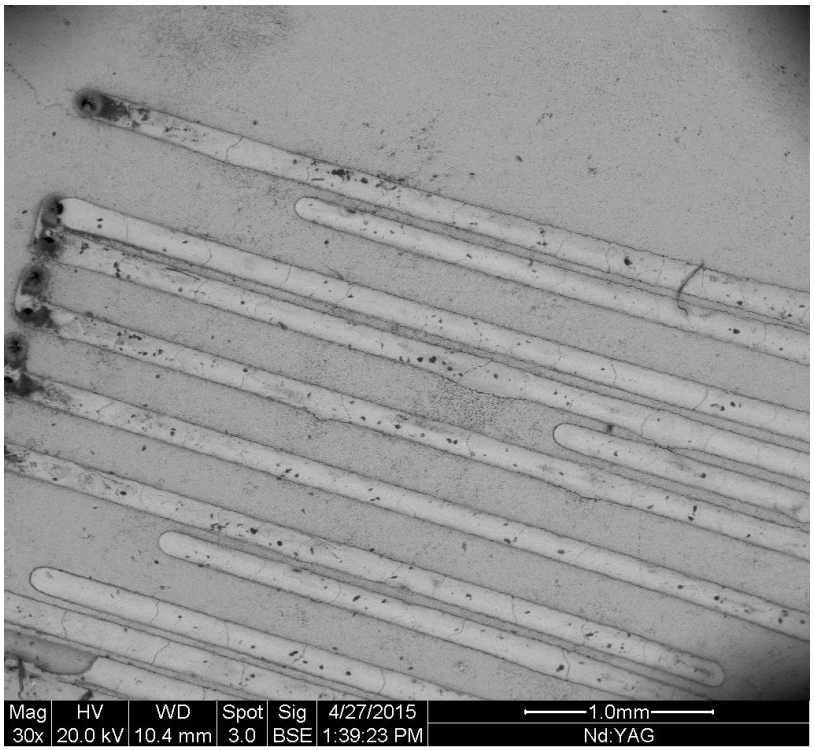

Figure 27. SEM image in BSE mode of $Y_{3.002}Al_{4.998}O_{12}$ exposed to focused fs-pulse laser radiation.

Figure 28 shows the cross section of the sample, with the laser-exposed region in the top right of the image. The densification caused by the laser exposure has penetrated approximately 33 μm into the surface of the sample and the shrinkage due to densification caused the channel to crack away from the bulk material. There appears to be an interconnected matrix within the densified region composed of high atomic number elements which corresponds to the high concentration of yttrium (Z=39) shown in the WDS map in Figure 30. This shrinkage and separation is also apparent in the higher magnification surface scan shown in Figure 29.

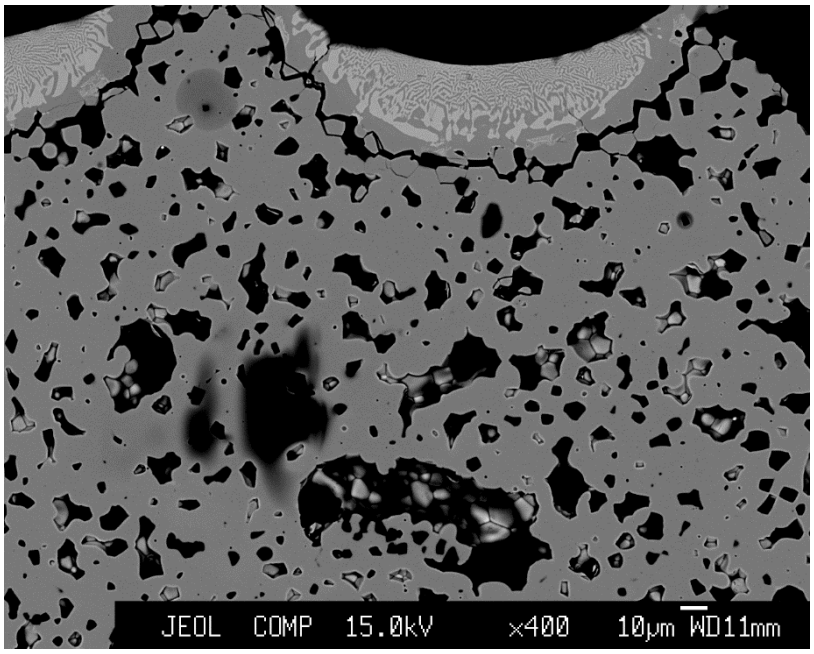

Figure 28. SEM image of YAG #10 ($Y_{3.002}Al_{4.998}O_{12}$) in cross-section revealing laser formed channel.

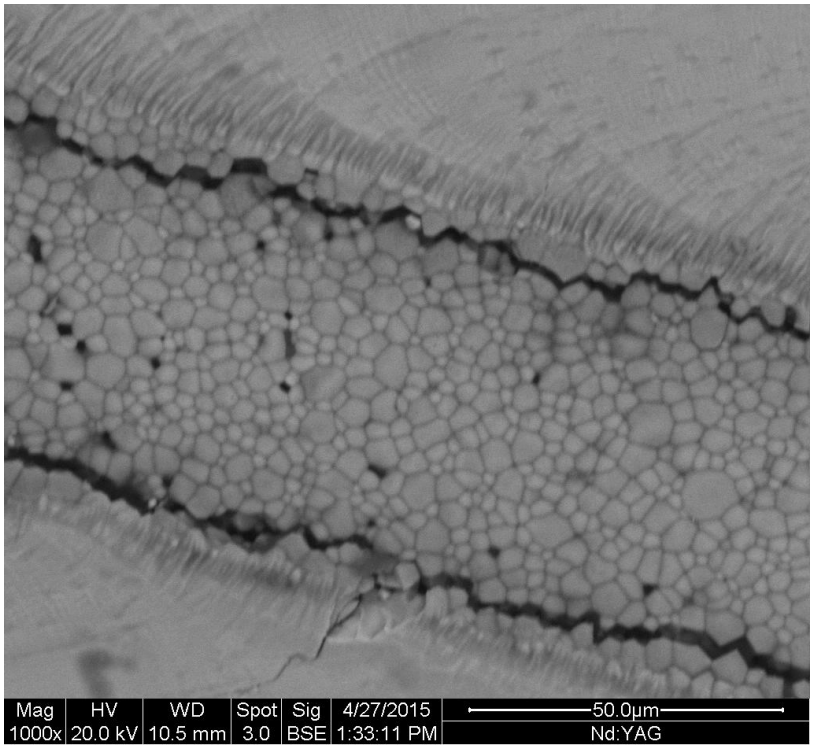

Figure 29. SEM image in BSE mode at 1000x of YAG #10 ($Y_{3.002}Al_{4.998}O_{12}$) showing densification, shrinkage and separation of laser exposed channels.

Figure 30 shows the relative concentrations of yttrium within the cross-section, Figure 31 shows the relative concentration of aluminum, and Figure 32 shows the relative concentration of oxygen. In each figure the dark blue areas correspond to porosity within the microstructure.

Figure 30 indicates a high relative concentration of yttrium within a clearly delineated region corresponding to the densified channel created by laser exposure. However, there is no corresponding reduction in concentration surrounding the high concentration region that would indicate diffusion of yttrium out of the bulk region to the densified one. The other elemental maps do not show any decrease in concentration in the dense region, so the reason for the increase in relative yttrium concentration is active interaction between the fs laser pulse and yttrium. These results demonstrate that the laser light can actively control the chemistry and thus optical or dielectric properties of of YAG ceramics.

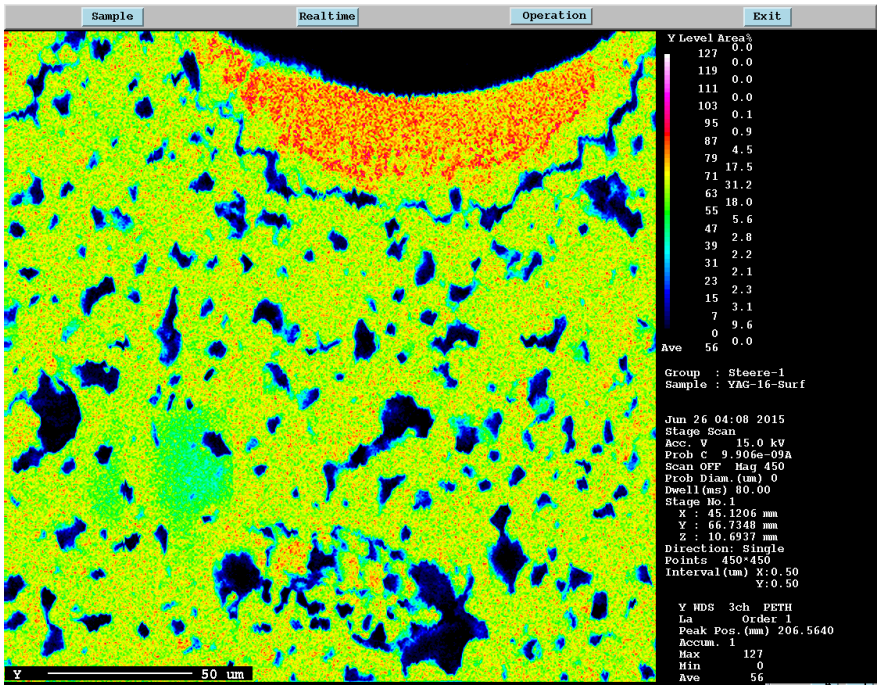

Figure 30. WDS map of laser exposed cross-section showing yttrium concentration.

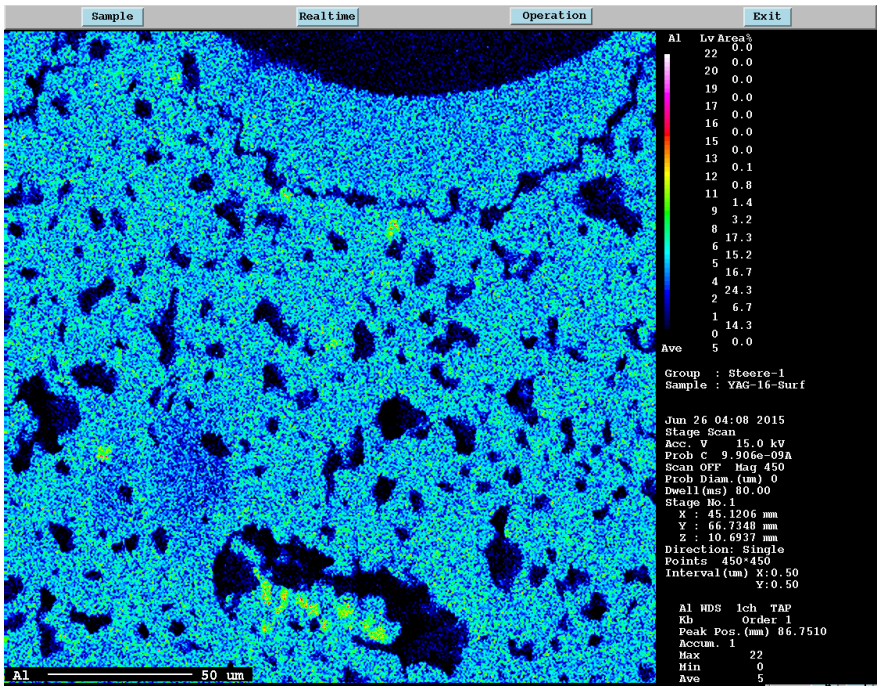

Figure 31. WDS map of laser exposed cross-section showing aluminum concentration.

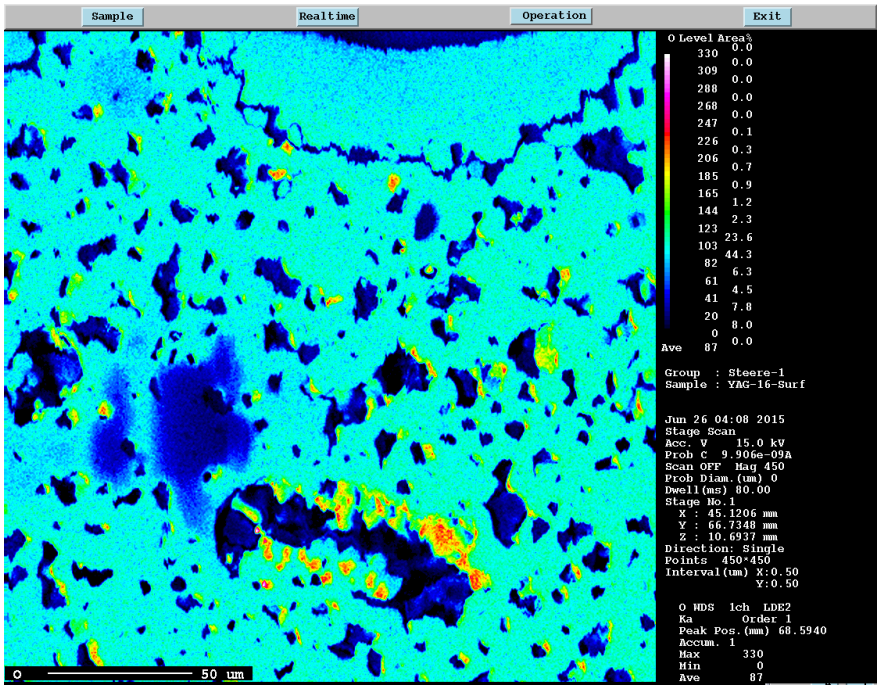

Figure 32. WDS map of laser exposed cross-section showing oxygen concentration.

b. Variable Rate Exposures

An opaque pellet of stoichiometric YAG ($Y_3Al_5O_{12}$) was exposed to the focused fs laser operating at an average power of 1.66 watts. Assuming a pulse duration of 40 fs based on the laser specification corresponds to a peak power of 8.14 MW. The width of the affected region for the different scan speeds was approximately 100 μm, an interaction area of 7.85×10^{-5} cm^2 resulting in a beam with calculated beam intensity at the sample surface of 103 GW/cm^2. The width of the surface features remains relatively constant at varying scan speeds, but at lower scan speeds there appears to be more ablation and debris from grains which have been separated from the surface. As the scan rate increases the apparent depth of the features decreases and the dominant result appears to be densification and shrinkage rather than ablation. Scan rates of 0.1 mm/s, 0.25 mm/s, and 0.5 mm/s display similar ablation behavior, and scan rates of 1.0 mm/s, 1.5 mm/s and 2.0 mm/s display similar densification behavior, indicating a threshold of energy absorption at rates between 0.5 mm/s and 1.0 mm/s. The SE-BSE images are shown in Figure 33.

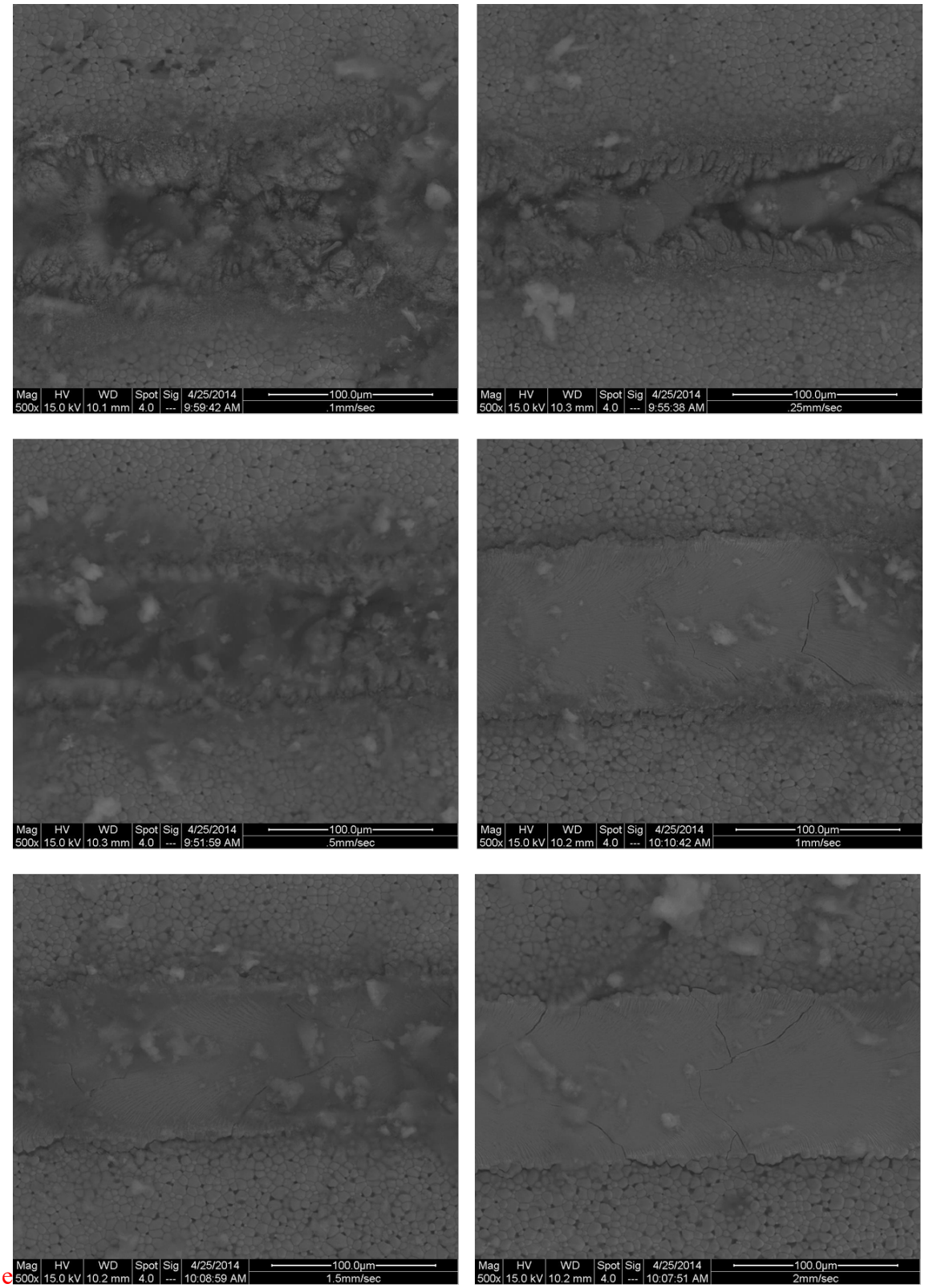

Figure 33. SE-BSE Images at 500x magnification of laser beam exposure paths.
Left to Right: 0.1 mm/s, 0.25 mm/s, 0.5 mm/s, 1.0 mm/s, 1.5 mm/s, 2.0 mm/s.

D. X-ray Diffraction Results

After sintering, all ten ceramic YAG samples were crystalline and matched the diffraction pattern for $Y_3Al_5O_{12}$ due to the small range of difference between the chemical compositions and stoichiometric YAG. Figure 34 shows a representative XRD pattern of one of the ceramic YAG compositions and the Miller indices corresponding to each diffraction peak.

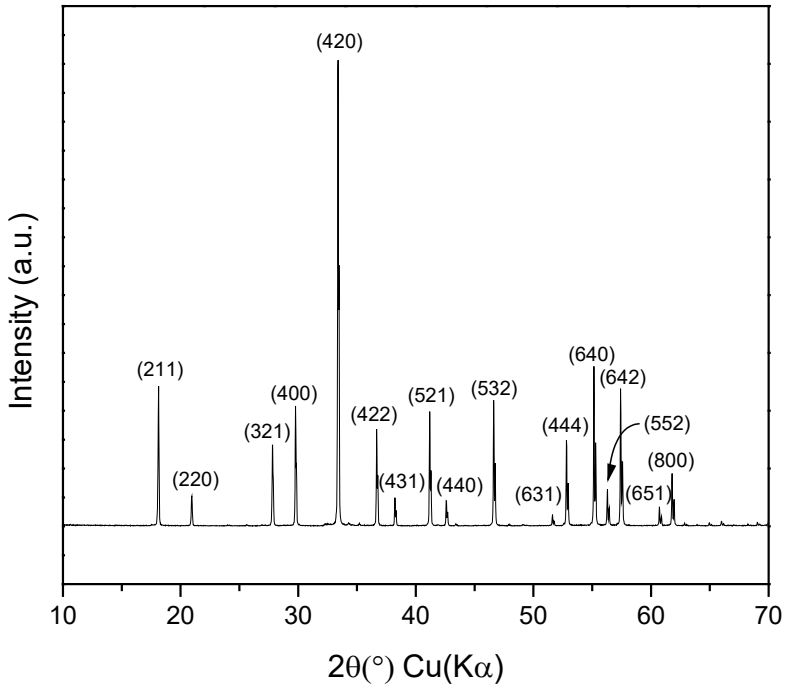

Figure 34. Representative XRD plot indicating the Miller indices of the phase pure YAG ceramics.

E. Grazing Incidence X-Ray Diffraction (GIXRD)

Figure 35 shows the GIXRD diffraction patterns for the sample of ceramic YAG ($Y_{3.002}Al_{4.998}O_{12}$) before and after exposure to the focused femtosecond laser pulse beam. The diffraction patterns show diffraction peaks at the same diffraction angles, but after exposure the intensity of the peaks increased. The dominant phase in both cases is YAG ($Y_3Al_5O_{12}$) with some residual yttrium oxide (Y_2O_3). Laser exposure appears to increase the intensity of the diffraction peaks by densifying the local microstructure of the sample surface on solidification.

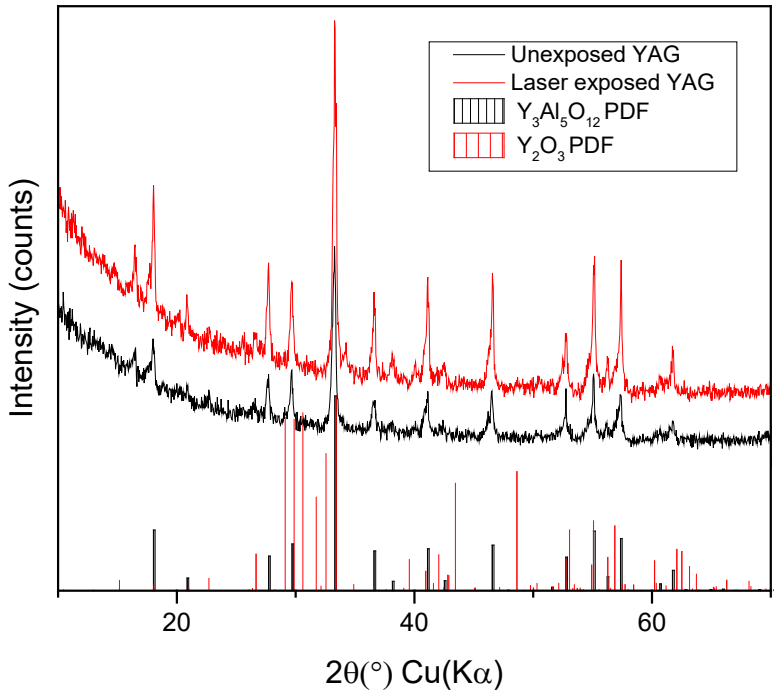

Figure 35. GIXRD pattern from YAG sample before and after fs pulse laser exposure.

F. THz Properties of Transparent YAG Ceramics

Figure 36 shows the THz spectra measured between approximately 0.003 and 2.5 THz. Each series is the average of three scans taken for each sample. All calculations were performed using data between 0.003 and 2.5 THz because above 2.5 THz the time domain signal fell below the noise floor of the measurement.

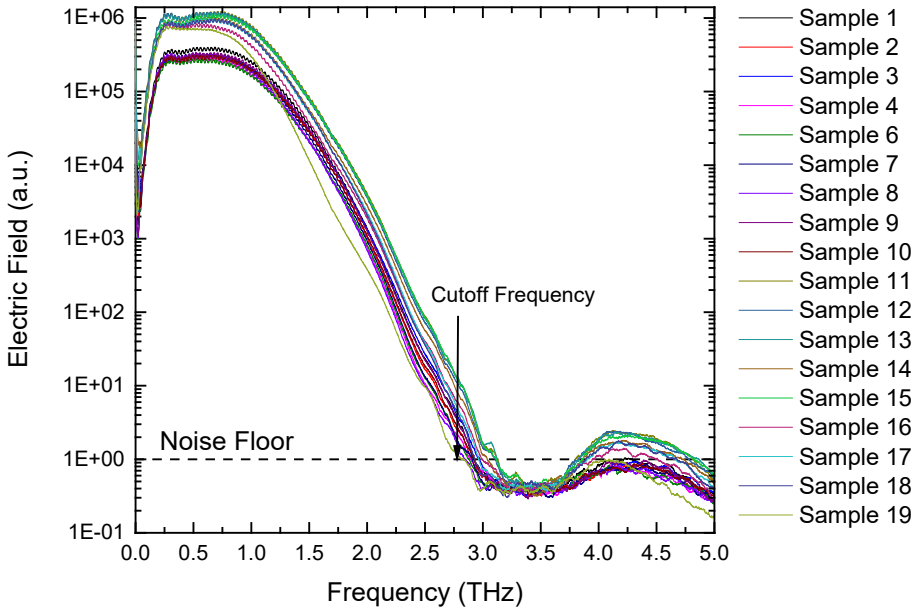

Figure 36. THz spectra for the entire range of Y-Al-O transparent compositions.

The absorption coefficient as a function of frequency for the transparent samples is shown in Figure 37. Most of the samples display similar properties, except for sample #19 ($Y_{3.077}Al_{4.923}O_{12}$) the most yttrium rich sample of the set. With the quantity of transparent YAG ceramics limited to one of each composition, the source of this shift is not attributable to chemistry or microstructure. The THz-TDS measurements were repeatable indicating a valid measurement.

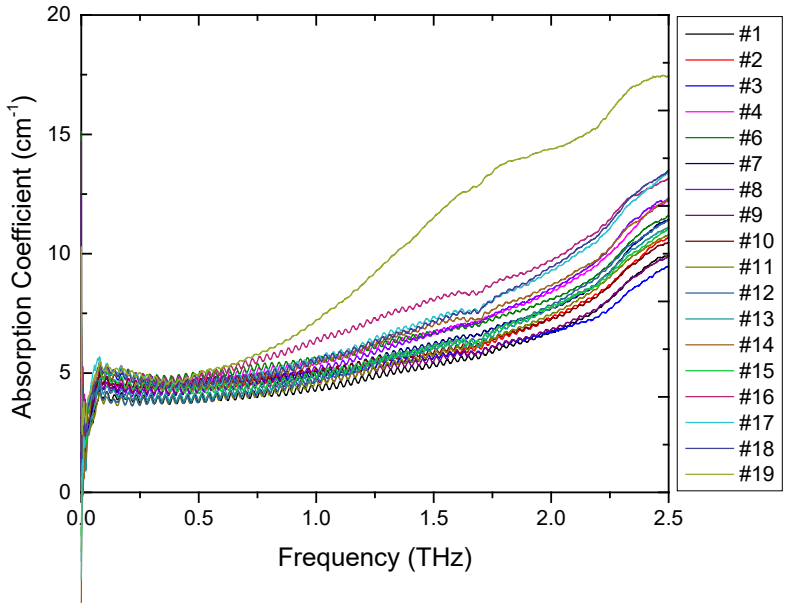

Figure 37. Absorption coefficients for chemically variant transparent YAG ceramics. Chemical compositions are listed in Table V.

Figure 38 shows a combined plot of the refractive indices and average grain diameter of the transparent YAG ceramics as a function of their departure from the stoichiometric YAG composition ($Y_3Al_5O_{12}$).

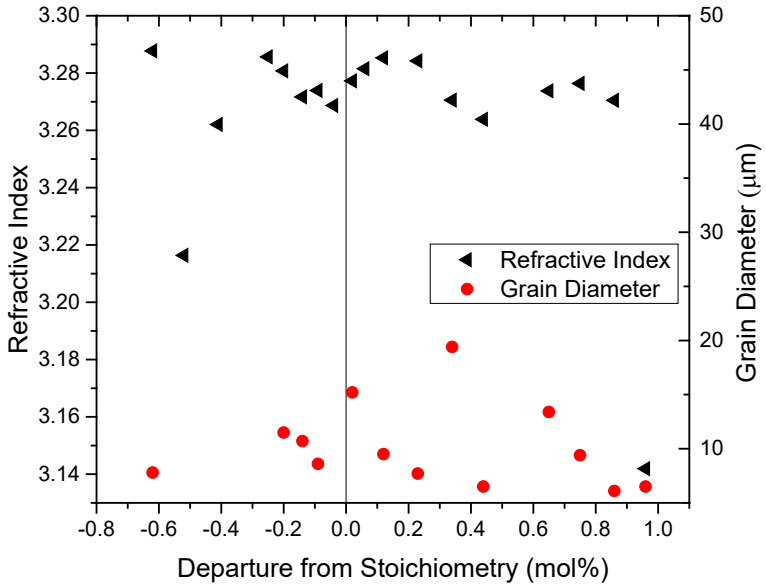

Figure 38. Refractive index at 0.75 THz of transparent YAG ceramics measured via THz-TDS. Average grain diameter calculated from SEM images.

I. Temperature Dependent THz-TDS Measurements

To further investigate the possibility of THz absorption via a phonon-difference process, the spectrum of an undoped YAG single crystal was measured as a function of temperature from 20 to 220°C. The resulting increase in absorbance with temperature is shown in Figure 39. The following section is an extract from *Effect of nonstoichiometry on the terahertz absorption of $Y_3Al_5O_{12}$ optical ceramics* published by Dr. Romain Gaume, Daniel Steere, and Dr. S.K. Sundaram in the Journal of Materials Research.[54]

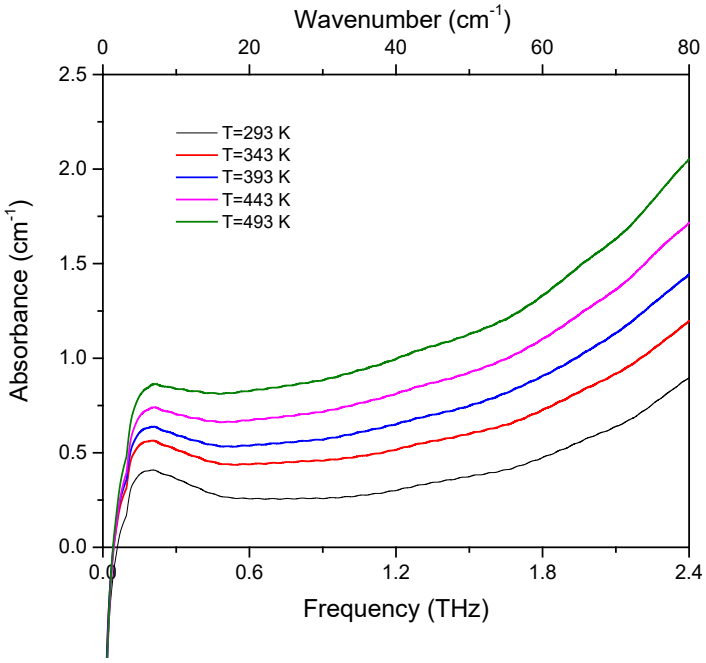

Figure 39. THz absorbance spectrum at different temperatures.

The absorption at $\nu_o = 3.5$ THz is temperature independent while the contribution of the main band increases with temperature. The absorbance of THz radiation can be explained by the product of three terms. The first one is the matrix element of the coupling term between the phonons involved in the process. It is non-zero only for specific phonon combinations determined by selection rules derived from symmetry considerations. The second one describes the temperature dependence of the phonon occupation number of the phonon states involved in the process and the third is related to the phonon density of state. Specifically, the net probability of optical absorption by a solid is proportional to the difference between stimulated phonon generation and absorption rates, $W_{n,n+1}$ and $W_{n,n-1}$ respectively:[55]

$$W_{n,n+1} = \left| \left\langle \psi_{n+1,N} \middle| H \middle| \psi_{n,N'} \right\rangle \right|^2 \sim n+1 \qquad (12)$$

$$W_{n,n-1} = \left| \left\langle \psi_{n,N} \middle| H \middle| \psi_{n-1,N'} \right\rangle \right|^2 \sim n \tag{13}$$

$$\langle n \rangle = \frac{1}{\exp\left(\hbar\omega / k_B T \right) - 1} \tag{14}$$

where H is the interaction Hamiltonian, n is the occupation state of the phonon and N is the quantum number of the THz photon field. <n> is the average phonon population density at a temperature T. A THz absorption process with generation of a single phonon is thus proportional to:

$$\left[\overline{n}(\omega) + 1 \right] - \overline{n}(\omega) = 1 \tag{15}$$

and, consequently, its amplitude is independent of temperature. Hence, the temperature independent absorption peak at 3.5 THz can be assigned to the absorption of a THz photon (**k**=**0**) and the creation of a single phonon associated to the translation of yttrium ions in their dodecahedral sites. In order to account for the temperature dependency of the main absorption band, one must invoke an optical absorption mediated by higher order photon-lattice interactions.[55,56] In compound crystals, such as YAG, such mechanisms are either induced by (i) second and higher order terms in the electric moment, or by (ii) the anharmonic coupling between phonons, arising from third and higher order terms in the potential energy. In process (i), where the first-order dipole moment can be zero, the photon couples directly with two phonons, the first one producing the asymmetry in the electronic charge distribution, which is then displaced by the second phonon. In process (ii), the anharmonic mechanism has been described by the coupling of a photon with a TO phonon, which subsequently couples with two other phonons. In either case, the net result can be the creation of two phonons (summation process) or the creation of one phonon and the

annihilation of the other (difference process). The centrosymmetry of the YAG lattice further implies that the two-phonon combinations must originate from two different branches and that overtones are forbidden. Here, because $\nu_o = 3.5$ THz corresponds to the lowest polar mode of the YAG lattice, only a high-order, two-phonon difference (2PD) process, involving mechanism (i) shown in Figure 40 can explain the absorbance below 3.5 THz.

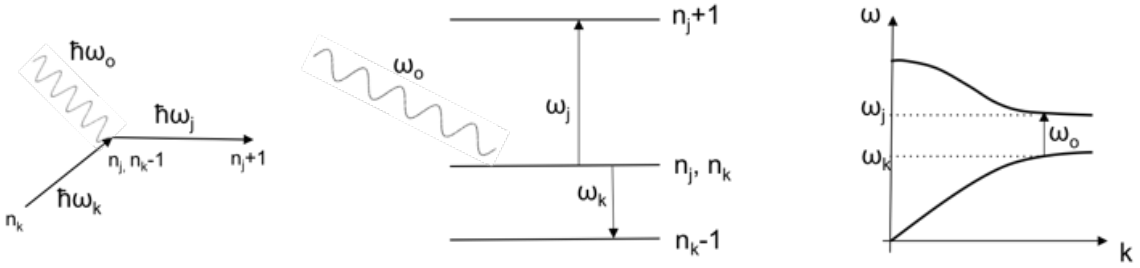

Figure 40. Two-phonon absorption and emission diagram.

Similarly to (1), the temperature dependency of the 2PD process of Figure 40 can be described by:

$$\left(\bar{n}_j(\omega_j)+1\right)\bar{n}_k(\omega_k)-\bar{n}_j(\omega_j)\left(\bar{n}_k(\omega_k)+1\right)=\bar{n}_k(\omega_k)-\bar{n}_j(\omega_j) \qquad (16)$$

In the high-temperature limit ($k_BT \gg \hbar\omega_k$), the absorbance is found to depend linearly with the temperature:[57-61]

$$\bar{n}_k(\omega_k)-\bar{n}_j(\omega_j)\approx\frac{\omega_o}{\omega_j}\cdot\frac{k_BT}{\omega_j+\omega_o} \qquad (17)$$

where ω_o and ω_j are the frequencies of the incident THz photon and of the acoustic phonon respectively. Above 350 K, the absorbance in the 1.5 to 2.6 THz spectral range follows a linear dependency with temperature as shown in Figure 41, confirming that the broad asymmetric absorption band arises from a 2PD process.

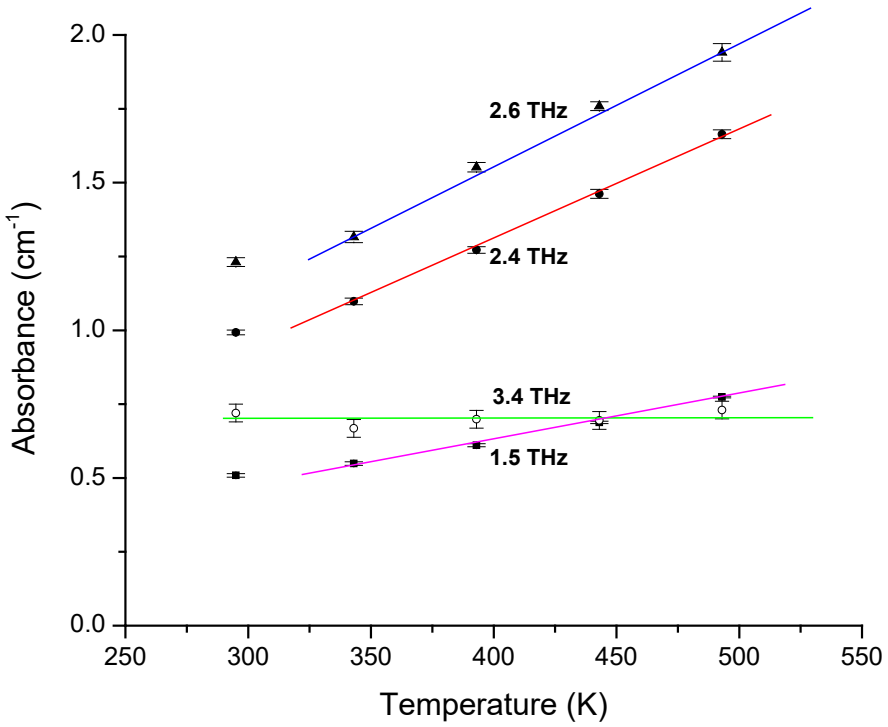

Figure 41. Linear relation between THz absorbance and temperature above 350 K.

G. THz Properties of Opaque YAG Ceramics

The THz frequency spectrum of an opaque YAG ceramic is shown in Figure 42. Before analyzing the refractive index and absorbance data, the cutoff frequency where the measured spectrum intensity fell below the noise floor of the measurement was determined for each sample[62]. Beyond this frequency the low signal to noise ratio results in an invalid input to the equations used to calculate the dielectric properties. For comparisons of refractive index and absorption coefficients between samples, the frequency of 0.75 THz was selected as it occurred below the cutoff frequency for all samples. The THz absorption coefficients for the chemically varied YAG ceramics are shown in Figure 43

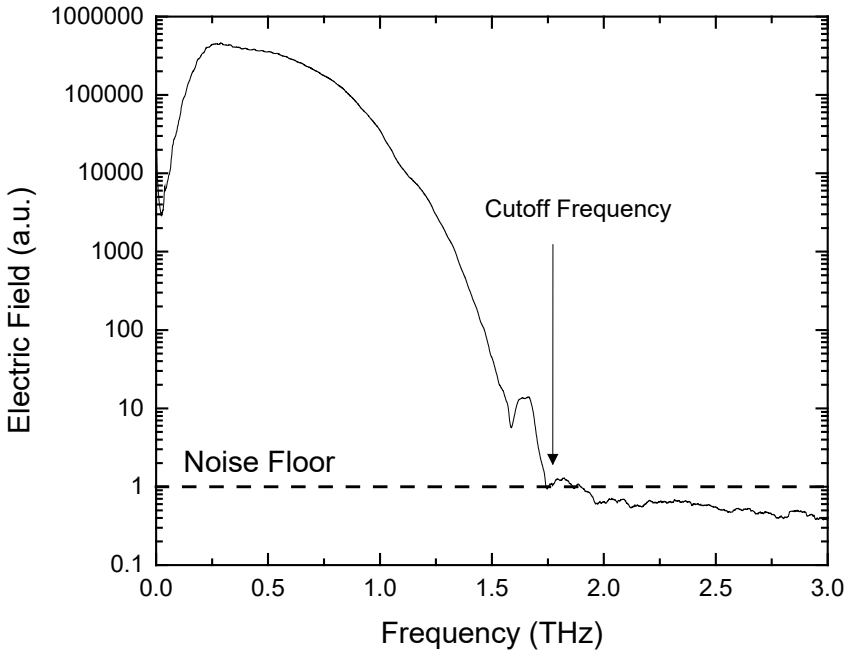

Figure 42. Frequency spectrum of an opaque YAG pellet, illustrating the cutoff frequency where the spectrum intensity decreases to the noise floor of the measurement.

Samples #9 ($Y_{2.997}Al_{5.003}O_{12}$) and #10 ($Y_{3.002}Al_{4.998}O_{12}$), the ceramics with chemistries closest to stoichiometry exhibit higher absorption coefficients than the samples shifted away from stoichiometry as shown in Figure 43. For all other samples except for numbers 9 and 10, absorption coefficient gradually increases with an upward curvature with frequency, but for the dense samples 9 and 10, the absorption coefficient initially increases rapidly with frequency but with a negative curvature.

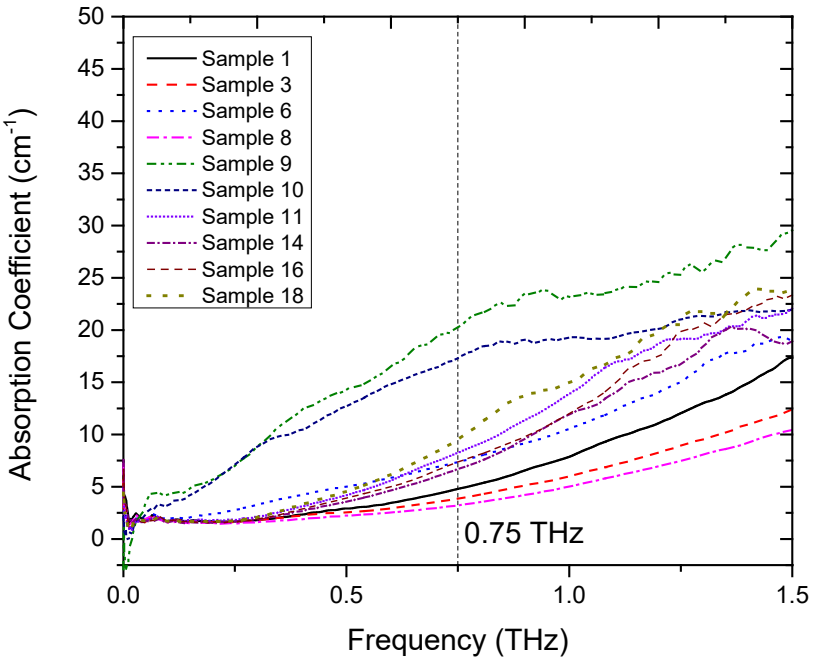

Figure 43. Absorption coefficients as a function of frequency for all ten selected opaque YAG ceramics. Dashed vertical line indicates frequency at which absorption coefficient and refractive index were compared.

Figure 44 shows the frequency dependence of the refractive index. The refractive index remains essentially constant over the frequency range up to the frequency cutoff at the noise floor. Sample 9 exhibits a high refractive index at low frequencies, but the rest of the frequency range exhibits similar behavior to the other samples, indicating that it is caused by an artifact of the measurement.

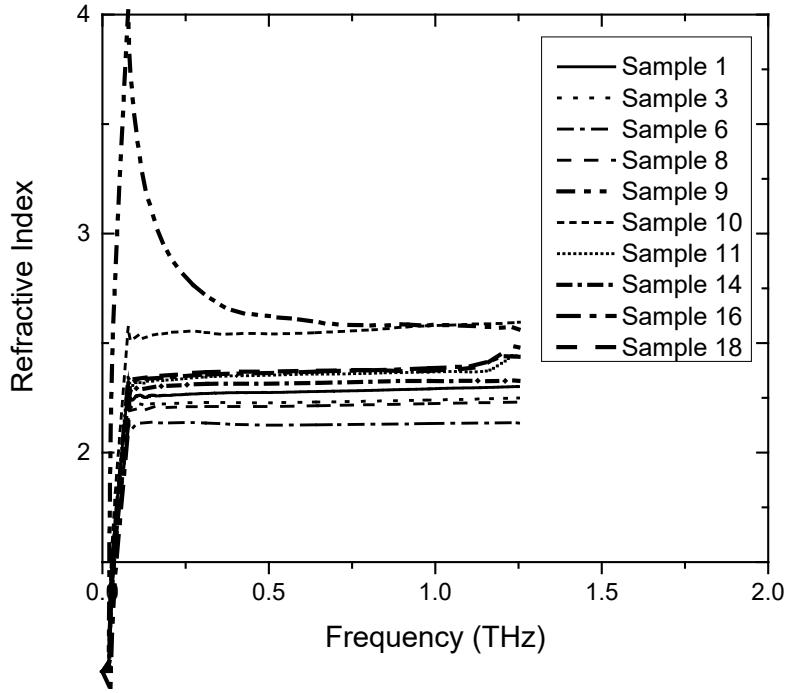

Figure 44. Refractive indices with respect to frequency for opaque ceramic YAG.

The dielectric constant was taken for each sample at 1.0 THz for the purpose of comparing the results as a function of sample density. Because of the porous nature of the sintered materials, the true material properties could not be directly measured. We modeled the dielectric constant as a function of bulk density using an equation independently developed by Landau and Lifshitz[63], and Looyenga[64], which implies that for a heterogeneous mixture, the cube roots of the permittivities for the mixture components are additive when taken in proportion to their volume fractions. Figure 45 shows the linear relationship between the bulk density and cubed root of the real dielectric constant at 1.0 THz. In this case the two components are the bulk $Y_3Al_3O_{12}$ material, and the atmospheric air contained in the porous network. This relationship is described in equation 18.

$$(\varepsilon)^{1/3} = v_1(\varepsilon_1)^{1/3} + v_2(\varepsilon_2)^{1/3} \quad (18)$$

By extrapolating the best fit linear relationship calculated in Figure 45 to the bulk densities of air (0.0012 g/cm^3 at 20 °C and 101.325 kPa) and YAG (4.56 g/cm^3) and cubing the results, the dielectric constant of air was calculated to be 0.88 compared to the actual value of 1.00, and the dielectric constant of 100% dense YAG was calculated to be 10.95

compared to the average value of 10.66 experimentally measured at 1.0 THz across the series of transparent fully dense YAG ceramics. There is a clear linear relationship with a best fit R-Square value of 0.99.

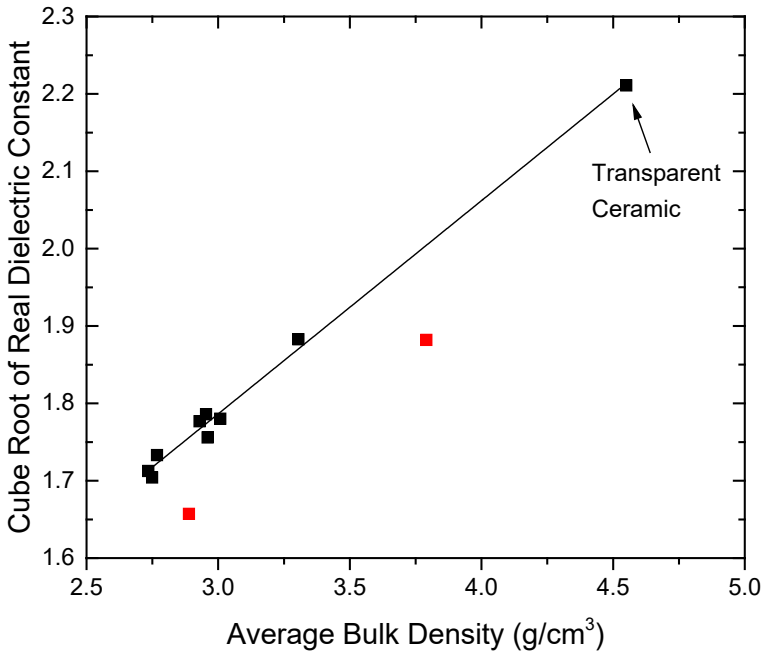

Figure 45. Cube root of dielectric constant as a function of sample bulk density at 1.0 THz.

Figure 46 and Figure 47 show refractive index and absorption coefficient plotted for comparison against average pore diameter and average bulk density, respectively. The properties trend similarly to the bulk density, while there is no readily apparent trend with average pore diameter.

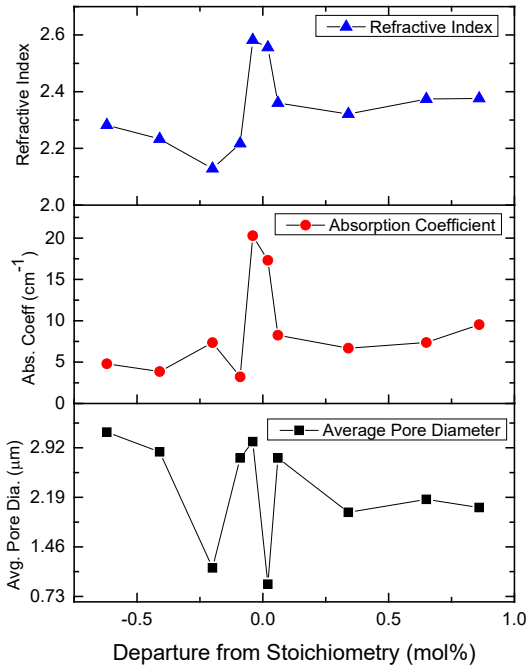

Figure 46. Refractive index and absorption coefficients compared between samples at 0.75 THz. Bottom graph shows average pore diameter measured using mercury porosimetry.

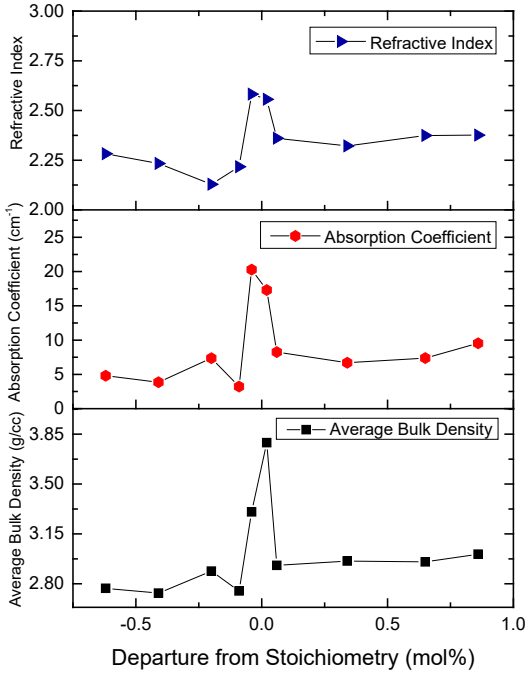

Figure 47. Refractive index and absorption coefficient plotted vs. sample stoichiometry. Bulk density is shown for comparison.

Figure 48 shows the absorption coefficients at 0.75 THz and average bulk density of the transparent YAG ceramics as a function of the departure from stoichiometry. The two samples closest to the stable $Y_3Al_5O_{12}$ stoichiometry show a dramatic increase in bulk density after sintering, with a corresponding increase in the absorption coefficient. In Figure 49, the absorption coefficient is plotted as a function of the bulk density and a best-fit linear relationship is calculated with an R-squared value of 0.7363.

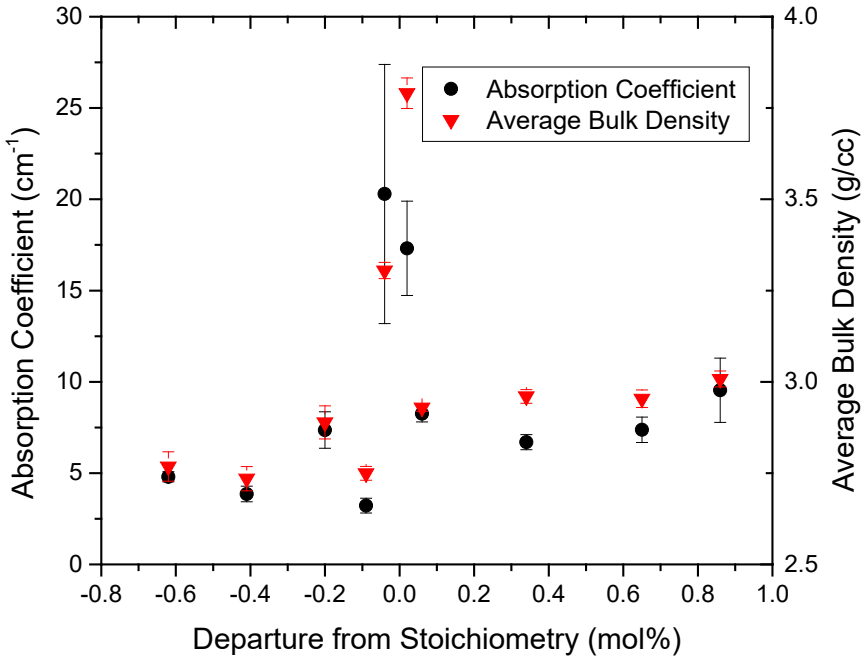

Figure 48. Absorption coefficient overlaid with bulk density as a function of departure from $Y_3Al_5O_{12}$ stoichiometry. Error is one standard deviation.

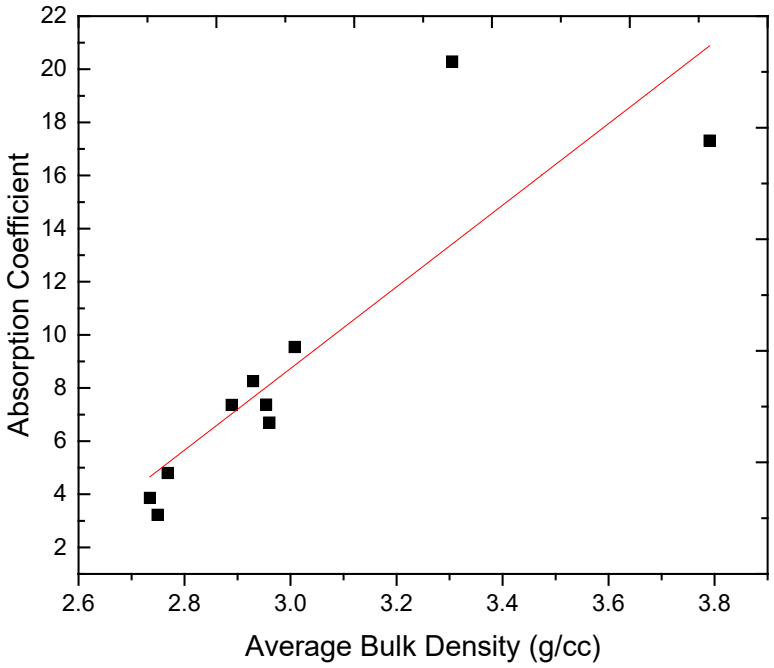

Figure 49. Absorption coefficient of opaque YAG ceramics as a function of the average bulk density of each sample.

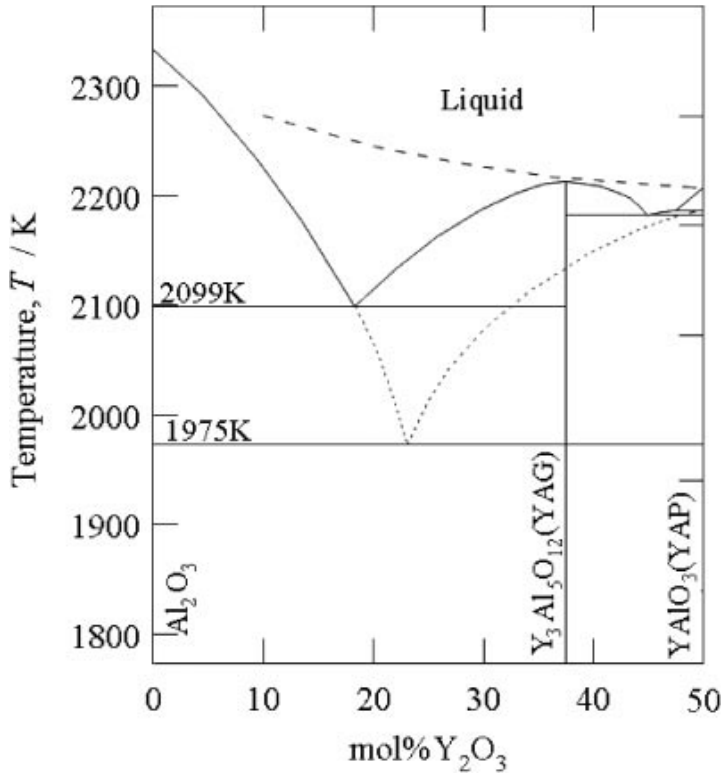

Figure 50. Phase Diagram of the Al_2O_3-Y_2O_3 system. The dotted lines indicate the liquidus of the metastable eutectic system. Melts cooled down from the temperatures above the dashed line (a) follow the metastable path of the solidification.[65]

H. Grain-size effects

Figure 51 shows the THz spectra for different sintering times. The apparent differences in amplitude and cutoff frequency are due to the variations in the sample thickness (between 1.64 mm and 2.1 mm in thickness). Thicker samples attenuate more of the THz pulse, resulting in a lower cutoff frequency. Thicker samples attenuate more of the THz pulse resulting in lower transmitted intensities. These variations are accounted for when calculating refractive index and absorption coefficients.

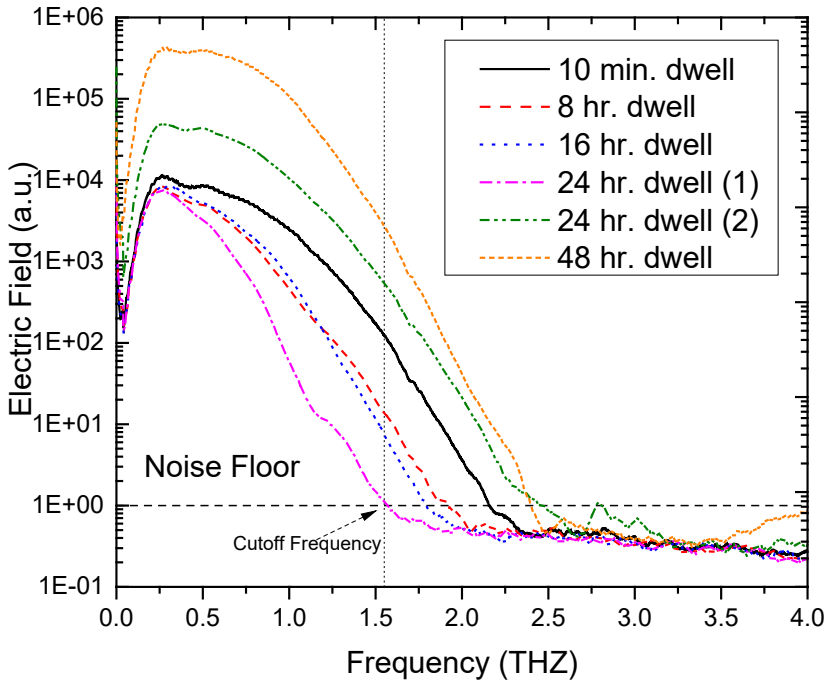

Figure 51. THz frequency spectrum for $Y_{3.002}Al_{4.998}O_{12}$ ceramics fired for different times to indicate the frequency range from 0.0 to 1.5 THz used for comparison.

Figure 52 shows the average refractive index for different sintering times. The sample fired for 10 minutes has a significantly lower refractive index over the entire spectrum due to its low density and high volume of entrapped air. The YAG pellet fired for 10 min exhibited the beginning stages of sintering with limited particle necking and small grains with diameters on the order of 1 μm. There was no apparent grain growth. The partially sintered grain matrix resulted in high degrees of connected bulk porosity. After 8 h of sintering at 1700°C grains had more completely bonded together, causing a reduction in porosity. Average grain diameter was around 2 μm, but with a reduction in porosity compared to the sample fired for 10 min, sintering up to 83% of theoretical density. Beyond 2 h dwell time, the sintered density plateaued at approximately 85% of theoretical density, regardless of sintering time. 16 h dwell and the first of two 24 h dwells showed larger grains, while the second 24 h dwell had smaller grains than the first. It is believed that this is due to variations in the precursor particle size. All samples were made from one precursor

batch, and it is possible that variations in particle size distribution within the batch had an effect on the final grain size of these samples.

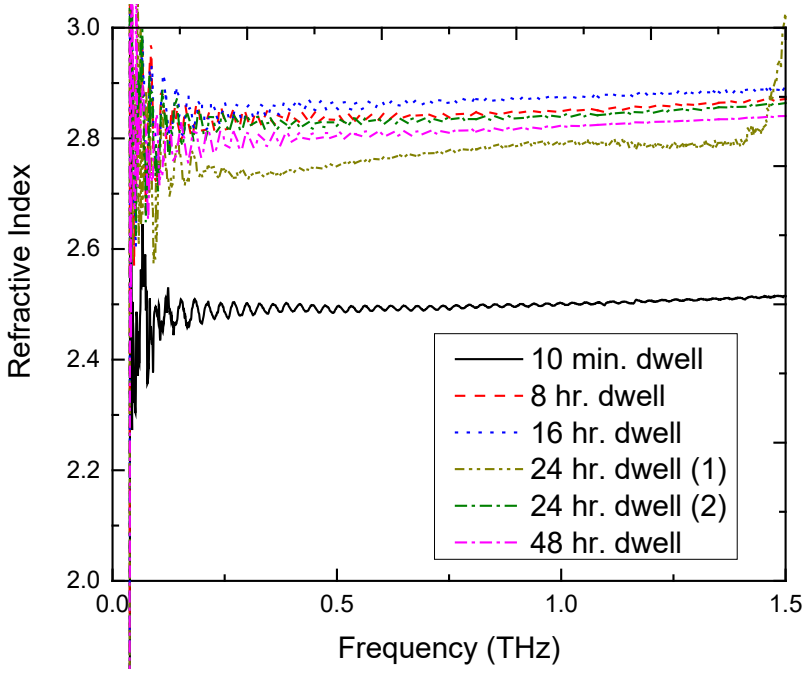

Figure 52. Refractive indices of $Y_{3.002}Al_{4.998}O_{12}$ ceramics fired at 1700 °C for varying dwell times.

To separate effects due to density or due to grain diameter, the refractive index at 0.75 THz was plotted as a function of both these properties as seen in Figure 53. As with absorption coefficient, the results show the refractive index increases linearly with increases in bulk density with a best-fit linear relationship with an R-squared value of 0.945. For the range of average grain diameters from 2 μm and up, the refractive index does not appear to scale with average grain diameter.

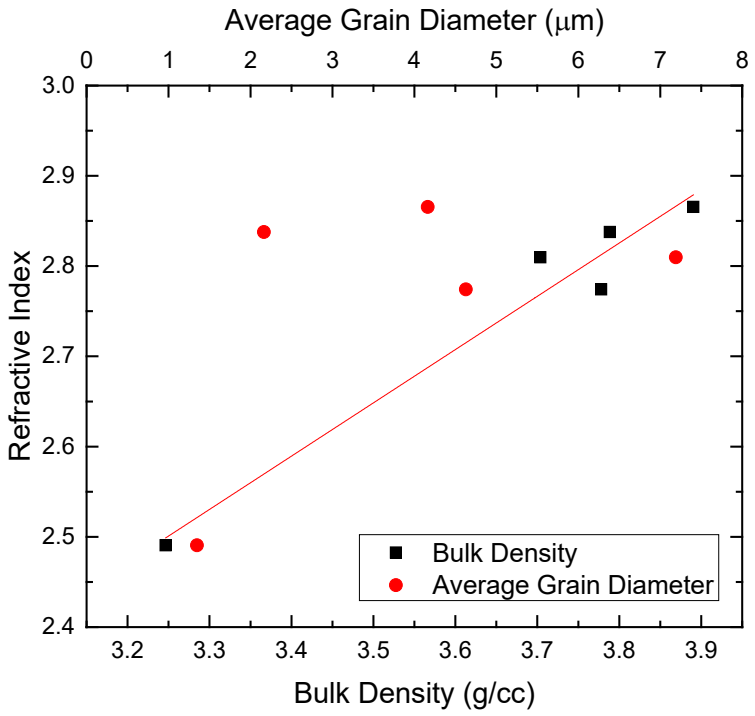

Figure 53. Refractive index at 0.75 THz as a function of bulk density, and of average grain diameter.

V. SUMMARY AND CONCLUSIONS

In summary, a number of YAG ceramic samples were prepared and characterized to test our proposed hypotheses. Selected samples were irradiated with concentrated fs pulse laser light operating at 800 nm, with a Gaussian beam shape and approximately less than 40 fs pulse duration. Some samples, due to the quality of their microstructures and lack of scattering sites, were transparent to visible light. At the laser beam intensities used in this thesis, these transparent materials exhibited non-destructive phenomena characteristic of short pulse laser interaction with high damage threshold transparent materials. Ablation and other forms of physical damage were not observed, however the materials did absorb the laser light, consequently emitting a range of visible frequencies resulting in a white light continuum. This is inconsistent with previous results found in literature that found the damage threshold for both pure and Nd-doped YAG to be lower than the intensities calculated here. This may be due to the fact that the calculated intensity is dependent on ideal specified values for the pulse duration and beam quality factor M^2, rather than values, which could be measured directly. Because of this limitation, the actual beam intensity incident upon the surface of the sample might be lower than the calculated value, and not exceed the ablation threshold.

Selected YAG samples which were uniaxially dry pressed at low pressures and sintered to 1700°C were fully opaque to visible light due to their high porosity and irregular grain boundaries which acted as scattering sites. The focal volume of the laser beam was scanned over the surface of the samples at a range of consistent speeds, and the results were observed with SEM. These materials did not transmit any light when exposed to the laser radiation, and did exhibit melting and re-solidification for short laser residence times. At longer irradiation times, ablation occurred resulting in the formation of deep cylindrical craters. In the areas where melting occurred, the fine grains of the original microstructure were consolidated into long narrow grains running perpendicular to the direction of the beam movement. The circular shape of the beam was also visible on the surface of the sample in the form of consecutive wavelike semi-circles visible along the beam path. Selective movement of the dopant (yttrium) from the matrix towards the focus point of the

fs laser beam energy was observed, indicating potential for active control of these materials.

THz-TDS was used to measure the optical and dielectric properties within a range of yttrium oxide/aluminum oxide chemical compositions precisely controlled above and below the stoichiometric YAG chemistry of $Y_3Al_5O_{12}$. Within this narrow range of yttrium oxide and aluminum oxide ratios, $-0.62 < \Delta\% < 0.96$, trends were observed indicating that between +/- 0.2 mol % the refractive index reached a local minima at the stoichiometric composition. Outside the range between +/- 0.2 mol %, it is hypothesized that randomly located inclusions of precipitated alumina-rich and yttria-rich phases within the YAG matrix resulted in variations in the dielectric properties. Calculation of the absorption coefficients also indicated a local minima at the stoichiometric phase composition, with increasing yttria content the absorption coefficient trended upwards, while for increasing alumina content the absorption coefficient increased to a maximum at a shift from stoichiometry of -0.25 mol %, at higher concentrations of alumina the absorption coefficient decreased.

A selection of Y-Al-O compositions was synthesized from chemical solutions and sintered, resulting in opaque ceramic disks. The dielectric properties of these samples were also studied using THz-TDS to compare with the transparent counterparts. It was found that between the microstructure variables of bulk density, pore volume and size distribution, grain size, and chemical composition, the bulk density had the most powerful effect on the optical and dielectric properties measured in the THz frequency range.

THz-TDS measurements of undoped single crystal YAG at varying temperatures revealed that the absorbance in the 1.5 to 2.6 THz spectral range followed a linear dependency with temperature, confirming that the broad asymmetric absorption band in these YAG samples arises from a 2PD process.

VI. FUTURE WORK

A. Laser System

For laser ablation studies, it is important that the sample be located so that the laser beam is focused directly on the surface and that the focal point of the beam is not in front of or behind the sample surface. Unmeasurable changes in the focus result in unknown variations in the spot size and laser fluence, which makes it difficult to analyze the results. In future work, it will be necessary to characterize the beam/sample interaction to achieve better control of the process variables. As seen in the work with opaque polycrystalline ceramics with non-uniform surfaces consisting of grain topography, surface voids and subsurface porosity, variations in the sample surface can affect the results of interaction with the laser beam. Areas with solid grains may show just a solid melt pattern or ablation crater, while areas with a thin coating over a subsurface void may melt away leaving a large hole. It would also be beneficial to characterize the exact region of the sample surface that will be exposed to the laser beam, so that the results can be correlated to the pre-exposure surface.

To better quantify the laser energy and fluence as it interacts with samples, it is necessary to know the pulse duration. Because the pulse durations are so short, it is not possible to use traditional electronics to measure the duration. An autocorrelator must be used to determine the pulse duration.

B. Sintering Mechanisms

It would be worthwhile to delve more deeply into the effect of stoichiometry on the sintering behavior of YAG, particularly under fs irradiation and in THz regime. General sintering of YAG has been extensively covered in other works and hence is not the focus of this thesis.

REFERENCES

1. J. E. Geusic, H. M. Marcos, and L. G. Van Uitert, "Laser Oscillations in Nd-Doped Yttrium Aluminum, Yttrium Gallium and Gadolinium Garnets," *Appl. Phys. Lett.,* **4** [10] 182-4 (1964).

2. W. Y. C. Yong-Nian Xu, "Electronic Structure of Yttrium Aluminum Garnet ($Y_3Al_5O_{12}$)," *Phys. Rev. B: Condens. Matter Mater. Phys.,* **59** [16] 530-5 (1999).

3. S. Kostíc, Z. Ž. Lazarević, V. Radojević, A. Milutinović, M. Romčević, N. Ž. Romčević, and A. Valčić, "Study of Structural and Optical Properties of Yag and Nd:Yag Single Crystals," *Mater. Res. Bull.,* **63** 80-7 (2014).

4. T. M. Baer and M. S. Keirstead, Spectra-Physics, Inc., "Nd-Yag Laser," United States Pat. 4,653,056 730,002, 1987.

5. J. Dong, P. Deng, F. Gan, Y. Urata, R. Hua, S. Wada, and H. Tashiro, "Highly Doped Nd:Yag Crystal Used for Microchip Lasers," *Opt. Commun.,* **197** 413-8 (2001).

6. J. E. Jackson and R. R. Rice, "Output Fluctuations of High Frequency Pulse Pumped Nd:Yag Laser," *J. Appl. Phys.,* **45** [5] 3 (1974).

7. Z. J. Kiss and R. J. Pressley, "Crystalline Solid Lasers," *Appl. Opt.,* **5** [10] 13 (1966).

8. M. P. Jianren Lu, Jianqiu Xu, Ken-ichi Ueda, "Highly Efficient 2% Nd:Yttrium Aluminum Garnet Ceramic Laser," *Appl. Phys. Lett.,* **77** [23] 3707-8 (2000).

9. G. A. Torchia, A. Rodenas, A. Benayas, E. Cantelar, L. Roso, and D. Jaque, "Highly Efficient Laser Action in Femtosecond-Written Nd:Yttrium Aluminum Garnet Ceramic Waveguides," *Appl. Phys. Lett.,* **92** [11] (2008).

10. R. Boulesteix, A. Maître, J.-F. Baumard, Y. Rabinovitch, and F. Reynaud, "Light Scattering by Pores in Transparent Nd:Yag Ceramics for Lasers: Correlations between Microstructure and Optical Properties," *Opt. Express,* **18** [14] 14992-5002 (2010).

11. K. Liu, D. He, H. Wang, T. Lu, F. Li, and X. Zhou, "High-Pressure Sintering Mechanism of Yttrium Aluminum Garnet ($Y_3al_5o_{12}$) Transparent Nanoceramics," *Scr. Mater.,* **66** 319-22 (2012).

12. R. Manalert and M. N. Rahaman, "Sol-Gel Processing and Sintering of Yttrium Aluminum Garnet (Yag) Powders," *J. Mater. Sci.,* **31** [13] 3453-8 (1996).

13. N. Frage, S. Kalabukhov, N. Sverdlov, V. Ezersky, and M. P. Dariel, "Densification of Transparent Yttrium Aluminum Garnet (Yag) by Sps Processing," *J. Eur. Ceram. Soc.,* **30** [16] 3331-7 (2010).

14. N. Frage, S. Kalabukhov, N. Sverdlov, V. Kasiyan, A. Rothman, and M. P. Dariel, "Effect of the Spark Plasma Sintering (Sps) Parameters and Lif Doping on the Mechanical Properties and the Transparency of Polycrystalline Nd-Yag," *Ceram. Int.,* **38** 5513-9 (2012).

15. M. K. Rachman Chaim, James Z. Shen, "Transparent Yttrium Aluminum Garnet (Yag) Ceramics by Spark Plasma Sintering," *J. Eur. Ceram. Soc.,* **27** 3331-7 (2007).

16. J.-F. Bisson, Y. Feng, A. Shirakawa, H. Yoneda, J. Lu, H. Yagi, T. Yanagitani, and K.-I. Ueda, "Laser Damage Threshold of Ceramic Yag," *Jpn. J. Appl. Phys.,* **42** 1025-7 (2003).

17. D. E. Zelmon, K. L. Schepler, S. Guha, D. Rush, S. M. Hegde, L. P. Gonzales, and J. Lee, "Optical Properties of Nd-Doped Ceramic Yttrium Aluminum Garnet," *Proc. SPIE,* **5647** 255-64 (2005).

18. J. B. Lonzaga, S. M. Avanesyan, S. C. Langford, and J. T. Dickinson, "Color Center Formation in Soda-Lime Glass with Femtosecond Laser Pulses," *J. Appl. Phys.,* **94** [7] 4332-40 (2003).

19. S. Besner, J.-Y. Degorce, A. V. Kabashin, and M. Meunier, "Influence of Ambient Medium on Femtosecond Laser Processing of Silicon," *Appl. Surf. Sci.,* **247** [1] (2005).

20. A. Borowiec and H. K. Haugen, "Femtosecond Laser Micromachining of Grooves in Indium Phosphide," *Appl. Phys. A,* **79** 521-9 (2004).

21. A. Cavalleri, K. Sokolowski-Tinten, J. Bialkowski, and D. V. d. Linde, "Femtosecond Laser Ablation of Gallium Arsenide Investigated with Time-of-Flight Mass Spectroscopy," *Appl. Phys. Lett.,* 72 [19] 2385-7 (1998).

22. S. Besner, A. V. Kabashin, F. M. Winnik, and M. Meunier, "Ultrafast Laser Based "Green" Synthesis of Non-Toxic Nanoparticles in Aqueous Solutions," *Appl. Phys. A*, 93 955-9 (2008).

23. L. Qi, K. Nishii, M. Yasui, H. Aoki, and Y. Namba, "Femtosecond Laser Ablation of Sapphire on Different Crystallographic Facet Planes by Single and Multiple Laser Pulses Irradiation," Optics and Lasers in Engineering, 48 1000-7 (2010).

24. L. Jiang and H. L. Tsai, in NSF workshop on "Unsolved Problems and Research Needs in Thermal Aspects of Material Removal Processes", Stillwater, OK, 2003.

25. C. B. Schaffer, A. Brodeur, and E. Mazur, "Laser-Induced Breakdown and Damage in Bulk Transparent Materials Induced by Tightly Focused Femtosecond Laser Pulses," *Meas. Sci. Technol.*, 12 1784-94 (2001).

26. M. D. Parrish, "The Creation of Micropatterns through the Femtosecond Laser Ablation of Diamond Materials"; Master's Thesis. University of Tennessee, 2009.

27. G. Nicolodelli, C. Kurachi, and V. S. Bagnato, "Femtosecond Laser Ablation Profile near an Interface: Analysis Based on the Correlation with Superficial Properties of Individual Materials," *Appl. Surf. Sci.*, 257 4 (2011).

28. S. H. Kim, I.-B. Sohn, and S. Jeong, "Ablation Characteristics of Aluminum Oxide and Nitride Ceramics During Femtosecond Laser Micromachining," *Appl. Surf. Sci.*, 255 4 (2009).

29. R. R. Gattass and E. Mazur, "Femtosecond Laser Micromachining in Transparent Materials," *Nat. Photonics*, 2 [4] 219-25 (2008).

30. T. H. Maiman, "Stimulated Optical Radiation in Ruby," *Nature*, 187 [4736] 493-4 (1960).

31. Femtosecond Laser Pulses: Principles and Experiments. Edited by C. Rullière. Springer-Verlag Germany, 1998.

32. Absorption and emission processes in two level system., J. Lamperski, Poznan University of Technology, 2005.

33. P. F. Moulton, "Ti-Doped Sapphire Tunable Solid State Laser," *Opt. News,* 8 [9] (1982).

34. R. Paschotta, in Encyclopedia of Laser Physics and Technology (R. Paschotta, ed.) Wiley-VCH, 2008.

35. E. G. Gamaly, A. V. Rode, V. T. Tikhonchuk, and B. Luther-Davies, "Ablation of Solids by Femtosecond Lasers: Ablation Mechanism and Ablation Thresholds for Metals and Dielectrics," *Phys. Rev. A*, 23 27 (2001).

36. B. N. Chichkov, C. Momma, S. Nolte, F. v. Alvensleben, and A. Tunnermann, "Femtosecond, Picosecond and Nanosecond Laser Ablation of Solids," *Appl. Phys. A*, 63 7 (1996).

37. S. K. Sundaram and E. Mazur, "Femtosecond Material Science - Inducing and Probing Nonthermal Transitions in Semiconductors," *Nat. Mater.*, 1 217-24 (2002).

38. "Terahertz Optics Taking Off," *Nat. Photonics*, 7, 665 (2013).

39. S. Kamba, D. Nuzhnyy, M. Savinov, J. Šebek, and J. Petzelt, "Infrared and Terahertz Studies of Polar Phonons and Magnetodielectric Effect in Multiferroic Bifeo3 Ceramics," *Phys. Rev. B: Condens. Matter Mater. Phys.*, 75 [2] (2007).

40. S. L. Dexheimer, Terahertz Spectroscopy, Principles and Applications. Edited by S. L. Dexheimer. 2008.

41. P. H. Siegel, "Terahertz Technology," *IEEE Trans. Microwave Theory Tech.*, 50 [3] 910-28 (2002).

42. M. Tonouchi, "Cutting-Edge Terahertz Technology," *Nat. Photonics*, 1 97-105 (2007).

43. R. A. Kaindl and R. D. Averitt, "Time-Resolved Thz Studies of Carrier Dynamics in Semiconductors, Superconductors, and Strongly-Correlated Electron Materials"; in Thz Spectroscopy: Principles and Applications. Edited by S. L. Dexheimer. Taylor & Francis CRC Press, 2007.

44. Y.-S. Jin, G.-J. Kim, and s.-G. Jeon, "Terahertz Dielectric Properties of Polymers," *J. Korean Phys. Soc.*, 49 [2] 5 (2006).

45. G. P. Gallerano, "Overview of Terahertz Radiation Sources"; pp. 216-21 in. Joint Accelerator Conferences Website,

46. H. Tuononen, E. Gornov, J. A. Zeitler, J. Aaltonen, and K.-E. Peiponen, "Using Modified Kramers-Kronig Relations to Test Transmission Spectra of Porous Media in Thz-Tds," *Opt. Lett.*, 35 [5] 3 (2010).

47. S. Ganti, "Characterization and Modeling of Laser Micro-Machined Metallic Terahertz Wire Waveguides"; Ph.D. Thesis. Wright State University 2012.

48. "Photonics Technical Note #1 Power Meters and Detectors," Newport, (2004).

49. "Test methods for laser beam widths, divergence angles and beam propagation ratios," ISO Standard 11146. International Organization for Standardization, Geneva, Switzerland.

50. "Standard Test Methods for Density of Compacted or Sintered Powder Metallurgy (PM) Products Using Archimedes' Principle," ASTM Designation B 962-08. American Society for Testing and Materials, West Conshohocken, PA.

51. "Standard Test Methods for Determining Average Grain Size," ASTM Designation E 112-10. American Society for Testing and Materials, West Conshohocken, PA.

52. R. Boulesteix, A. Maître, J.-F. Baumard, C. Sallé, and Y. Rabinovitch, "Mechanism of the Liquid-Phase Sintering for Nd:Yag Ceramics," *Opt. Mater.*, 31 [5] 711-5 (2009).

53. S. Choudhury, A. S. Gandhi, and V. Jayaram, "Bulk, Dense, Nanocrystalline Yttrium Aluminum Garnet by Consolidation of Amorphous Powders at Low Temperatures and High Pressures," *J. Am. Ceram. Soc.*, 86 [2] 247-51 (2004).

54. R. Gaume, D. Steere, and S. K. Sundaram, "Effect of Nonstoichiometry on the Terahertz Absorption of Y3al5o12 Optical Ceramics," *J. Mater. Res.*, 29 [19] 2338-43 (2014).

55. J. M. Ziman, "Phonon-Phonon Interaction"; p. 134 in Electrons and Phonons. Clarendon Press, Oxford, 1960.

56. E. Burnstein, "Interactions of Phonons with Photons: Infrared, Raman and Brillouin Spectra"; in Phonons and Phonon Interactions. Edited by T. A. Bak and B. N. Brockhouse. W.A. Benjamin, New York, NY, 1964.

57. H. Lengfellner and K. F. Ren, "Far-Infrared Laser Spectroscopy of Phonon Difference Band Absorption in Tlcl," *Z. Phys. B - Cond. Mat.*, 39 11-4 (1980).

58. H. Lengfellner, R. Rindt, and K. F. Ren, "Detection of Acoustic Zone-Boundary Phonons by Phonon Difference Absorption," *J. Phys.*, 12 [42] C6-259 (1981).

59. G. A. Komandin, O. E. Porodinkov, I. E. Spector, and A. A. Volkov, "Multiphonon Absorption in a Mgo Single Crystal in the Terahertz Range," *Phys. Sol. Stat.*, 51 [10] 2045-50.

60. R. Stolen and K. Dransfeld, "Far-Infrared Lattice Absorption in Alkali Halide Crystals," *Phys. Rev.*, 139 [4A] (1965).

61. R. H. Stolen, "Temperature Dependence of Far-Infrared Absorption in Gaas," *Phys. Rev. B*, 11 [2] 767-70 (1975).

62. B. M. F. Peter Uhd Jepsen, "Dynamic Range in Terahertz Time-Domain Transmission and Reflection Spectroscopy," *Opt. Lett.*, 30 [1] 29-31 (2005).

63. L. D. Landau and E. M. Lifshitz, Electrodynamics of Continuous Media. Pergamon Press, 1960.

64. H. Looyenga, "Dielectric Constants of Heterogeneous Mixtuers," *Physica*, 31 [3] 401-6 (1965).

65. J. L. Caslavsky and D. J. Viechnicki, "Melting Behaviour and Metastability of Yttrium Aluminium Garnet (Yag) and Yalo3 Determined by Optical Differential Thermal Analysis," *J. Mater. Sci.*, 15 [7] 1709-18 (1980).

APPENDIX

A. SEM for Grain Size Analysis

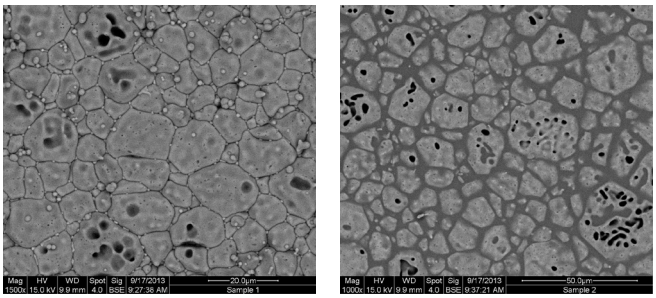

Figure 54. SEM images for Sample 1, $Y_{2.95}Al_{5.05}O_{12}$ and Sample 2, $Y_{2.958}Al_{5.042}O_{12}$ for grain size measurements.

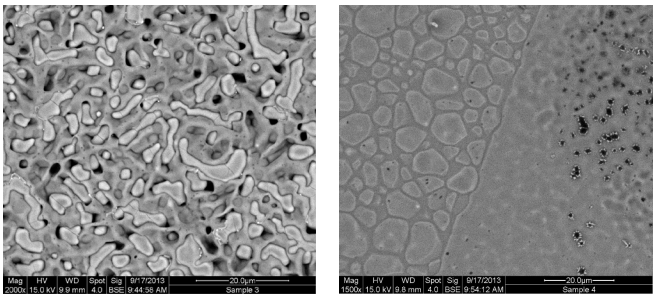

Figure 55. SEM image for Sample 3, Y2.967Al5.033O12 and Sample 4, Y2.98Al5.02O12 for grain size measurements.

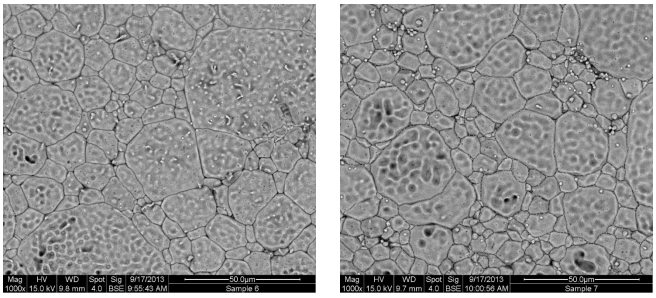

Figure 56. SEM image for Sample 6, $Y_{2.984}Al_{5.016}O_{12}$ and Sample 7, $Y_{2.989}Al_{5.011}O_{12}$ for grain size measurements.

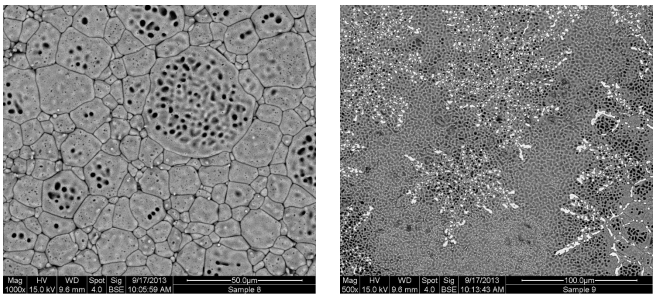

Figure 57. SEM image for Sample 8, $Y_{2.993}Al_{5.007}O_{12}$ and Sample 9, $Y_{2.997}Al_{5.003}O_{12}$ for grain size measurements.

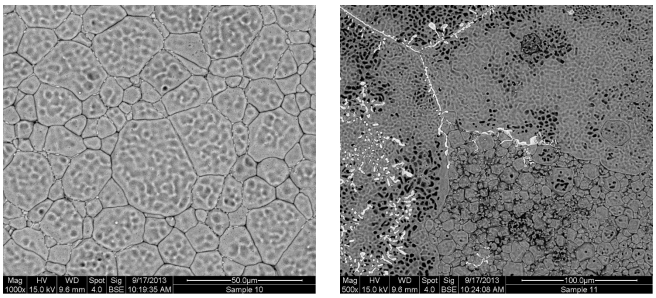

Figure 58. SEM image for Sample 10, $Y_{3.002}Al_{4.98}O_{12}$ and Sample 11, $Y_{3.005}Al_{4.995}O_{12}$ for grain size measurements.

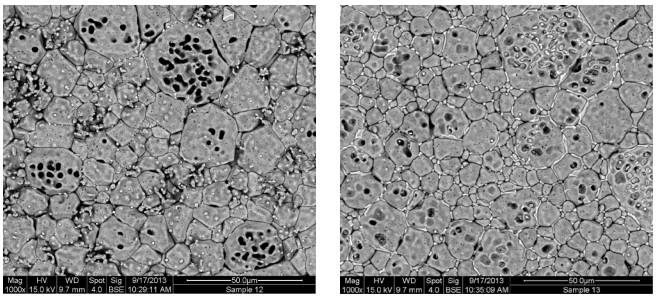

Figure 59. SEM image for Sample 12, $Y_{3.01}Al_{4.99}O_{12}$ and Sample 13, $Y_{3.018}Al_{4.982}O_{12}$ for grain size measurements.

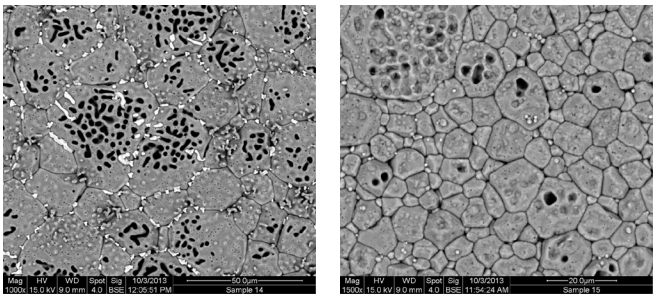

Figure 60. SEM image for Sample 14, $Y_{3.027}Al_{4.973}O_{12}$ and Sample 15, $Y_{3.035}Al_{4.965}O_{12}$ for grain size measurements.

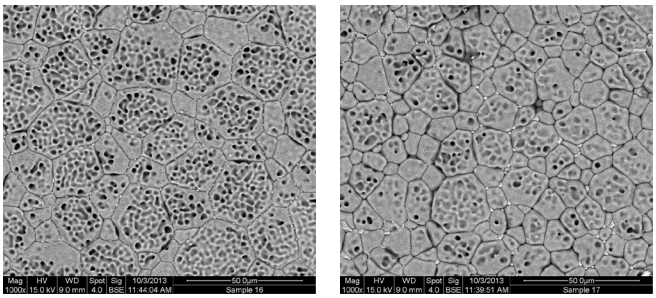

Figure 61. SEM image for Sample 16, $Y_{3.052}Al_{4.948}O_{12}$ and Sample 17, $Y_{3.06}Al_{4.94}O_{12}$ for grain size measurements.

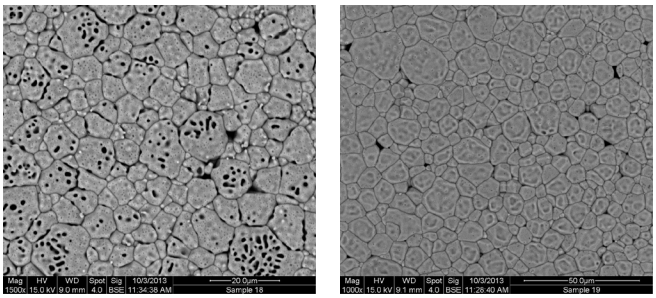

Figure 62. SEM image for Sample 18, $Y_{3.069}Al_{4.931}O_{12}$ and Sample 19, $Y_{3.077}Al_{4.923}O_{12}$ for grain size measurements.